

# Growth Factor-Loaded Mesoporous Silica Particles, Incorporated in Electrospun PCL Fibres, Provide Topographical and Chemical Cues for Tendon Tissue Engineering

Vera Citro, Marta Clerici, Matthew T. Shephard, Tina P. Dale,\* Aldo R. Boccaccini,\* and Nicholas R. Forsyth\*

This study develops a biomaterial-based strategy to address challenges in controlled growth factor delivery for tenogenic differentiation of mesenchymal stromal cells (MSCs) and tendon stem cells (TSCs). The 20% polycaprolactone (PCL) fibres, electrospun from acetic acid (AA) or formic acid:acetic acid (FA:AA) solutions, are loaded with bovine serum albumin (BSA) to evaluate initial protein-solvent interactions. SEM characterization demonstrated that fibres from AA has larger diameters ( $391 \pm 0.2$  nm) than those from FA:AA ( $282 \pm 0.5$  nm), with a further increase in diameter upon BSA incorporation. ATR-FTIR analysis confirmed successful protein loading but associated structural changes, particularly in AA fibres. Mesoporous silica nanoparticles (MSNs) are then optimized to encapsulate the model biomolecules BSA, lysozyme, and GDF-7, achieving high encapsulation efficiencies (80–100%) and sustained release due to electrostatic affinity. The MSNs, incorporated into aligned PCL fibres, better protect biomolecule stability and demonstrate uniform distribution, confirmed by SEM-EDS. Functional cell-based assays reveal good cell viability and metabolic activity for MSCs and TSCs cultured on the fibres, further enhanced under physoxic conditions (2% O<sub>2</sub>). The scaffold, integrating aligned fibres and MSNs, provides a biomimetic 3D structure for controlled cell alignment and tissue formation. This system offers tuneable drug delivery and shows potential as an autograft alternative for tendon regeneration.

facilitating motion and maintenance of posture.<sup>[1]</sup> The tendon's fibrillar extracellular matrix (ECM) is uniquely structured to withstand repetitive tensile forces, effectively transmitting and absorbing these stresses without incurring damage. This capability stems from the collagen fibre hierarchy's highly organized axial, longitudinal arrangement, which serves as a framework for cell and macromolecule attachment.<sup>[2]</sup> Beyond its biomechanical role, the ECM generates biochemical and mechanical signals that work together to regulate tenocyte behaviours, such as proliferation, survival, differentiation, and migration. These coordinated functions are crucial for maintaining the proper synthesis and assembly of the ECM, preserving tendon integrity and functionality.<sup>[3]</sup>

Tissue engineering utilises life sciences and engineering tools to create structures resembling those in the body. Using scaffolds, cells, and instructional cues, including growth factors, these elements help restore, sustain, or enhance

the function of the tendon when introduced into the body, providing a temporary template within the native biological environment, and promoting the gradual substitution with natural in situ-made structures.<sup>[4]</sup> Tenocytes are the most utilized

## 1. Introduction

Tendons are hierarchically organized, dense connective tissues that transmit forces generated by muscles to the skeleton,

V. Citro, M. Clerici, M. T. Shephard, T. P. Dale, N. R. Forsyth  
School of Pharmacy and Bioengineering  
Keele University  
Stoke-on-Trent, Staffordshire ST4 7QB, UK  
E-mail: [t.p.dale@keele.ac.uk](mailto:t.p.dale@keele.ac.uk); [nicholas.forsyth@abdn.ac.uk](mailto:nicholas.forsyth@abdn.ac.uk)



The ORCID identification number(s) for the author(s) of this article can be found under <https://doi.org/10.1002/admt.202500246>

© 2025 The Author(s). Advanced Materials Technologies published by Wiley-VCH GmbH. This is an open access article under the terms of the [Creative Commons Attribution](#) License, which permits use, distribution and reproduction in any medium, provided the original work is properly cited.

DOI: 10.1002/admt.202500246

V. Citro, A. R. Boccaccini  
Institute for Biomaterials  
Department of Materials Science and Engineering  
Friedrich-Alexander-University of Erlangen-Nürnberg  
91058 Erlangen, Germany  
E-mail: [aldo.boccaccini@fau.de](mailto:aldo.boccaccini@fau.de)

N. R. Forsyth  
Vice Principals' Office  
University of Aberdeen  
Kings College  
Aberdeen AB24 3FX, UK

cell source for tendon tissue engineering to replicate the natural tendon environment due to these cells being the most similar in terms of biology and mechanical properties. Nevertheless, obtaining tenocytes can be challenging, resulting in donor morbidity<sup>[5]</sup> and limitations in cell culture output.<sup>[6]</sup> A widely used alternative to tenocytes is undifferentiated cells, such as mesenchymal stromal cells (MSCs) and tendon stem cells (TSCs).

Different strategies have been used to induce MSCs and TSCs differentiation into tenocytes,<sup>[7–11]</sup> illustrating the parameters to consider during the design of a tendon tissue engineering scaffold. Cell-scaffold interaction, soluble signals, topographical cues and substrate mechanical properties have been identified as factors to consider recapitulating the major features of the native extracellular matrix at a multiscale level, guaranteeing the maintenance of a tendon-specific cell phenotype.<sup>[12]</sup>

Electrospinning has emerged as a pivotal technique in tissue engineering due to its ability to fabricate nanofibrous scaffolds via the uniaxial elongation of a viscoelastic jet derived from a polymer solution or melt.<sup>[13]</sup> This technique employs electrostatic repulsion, induced by an externally applied electric field, to continuously reduce the jet's diameter.<sup>[14]</sup> Consequently, this contactless process facilitates the fabrication of finer fibres, making it particularly advantageous for the production of hierarchical ECM-similar structures.<sup>[15]</sup> Additionally, electrospinning allows for the incorporation of bioactive molecules, enhancing cellular responses and promoting tissue regeneration.<sup>[16,17]</sup>

Here, electrospinning with a cylindrical collector was used to produce polycaprolactone (PCL) aligned fibres. To combine the topographical cue with a biochemical stimulus, we proposed a model in which fibres were utilised as a growth factor delivery system. Several growth factors, including insulin-like growth factor (IGF),<sup>[18]</sup> platelet-derived growth factor (PDGF),<sup>[19]</sup> basic fibroblastic growth factor (bFGF),<sup>[20]</sup> bone morphogenetic proteins (BMP),<sup>[21]</sup> transforming growth factor beta (TGF- $\beta$ ),<sup>[22]</sup> and vascular endothelial growth factor (VEGF)<sup>[23]</sup> are involved during both tendon ontogeny and healing responses. Among them, growth differentiation factor (GDF)-7 has proven to have an effective differentiation potential,<sup>[24]</sup> excluding any other undesired differentiation outcomes.

It is well established that the maintenance of protein tertiary structure is essential to its biological activity;<sup>[25]</sup> therefore, direct electrospinning of water-soluble proteins in polymer solution requires delicate mixing and inevitably results in denaturation of the bioactive agents as a consequence of the contact with organic solvents.<sup>[26]</sup> In preliminary studies, BSA tertiary structure was investigated after direct mixing with the polymeric solution obtained in two solvent systems, namely acetic acid (AA) and formic acid:acetic acid (FA:AA). Since both systems affected the BSA tertiary structure, we proposed here the use of mesoporous silica nanoparticles (MSNs) as an intermediate carrier. MSNs can be considered nanocontainers due to their large specific surface area, simple surface chemistry modification, uniform pore size distribution, adjustable pore network features, pore size between 2 and 50 nm, and good biocompatibility without negative effects.<sup>[27]</sup>

The use of MSNs expands the capability of electrospinning to deliver a bioactive product by protecting the fragile growth factors from the stress of electrospinning processing by confining it into

the particle porous structure. To assess the ability of the particles to protect the activity of biologically active molecules, even after the electrospinning procedure, lysozyme, with similar properties to GDF-7, was used. The data showed that the released lysozyme was biologically active and that this system can be further developed for the encapsulation of GDF-7. Cytotoxicity and cell viability were finally performed on both MSCs and TSCs, confirming the good interaction with both cell types.

## 2. Result

### 2.1. Successful Protein Encapsulation in Electrospun Fibres Depends on the Interaction with the Solvent

To test the potential of incorporating drugs in electrospun fibres we first utilised BSA as a model protein. BSA (3% polymer mass) was dissolved in a 20% PCL solution of either AA or FA:AA. BSA solubility in FA:AA was higher compared to AA alone, resulting in a transparent, homogenous solution (**Figure 1a**). Aligned and random fibres were obtained from both compositions. A statistically significant reduction in fibre diameter was found when AA solution was substituted with FA:AA (7:3), from  $391 \pm 0.2$  nm to  $255 \pm 0.1$  nm (**Figure 1b**). The incorporation of BSA into the polymeric solution resulted in further increases in fibre diameter across both solvent systems, with a 40% increase for fibres in AA and 50% for fibres in FA:AA (**Figure 1b**). The extent of PCL fibre alignment was assessed by measuring the angular difference between a centrally identified fibre (assigned as  $0^\circ$ ) relative to neighbouring fibres in the sample. Aligned fibre samples showed the highest concentration of fibres within a  $\pm 30^\circ$  angle. Conversely in the random groups, fibre orientation was uniformly distributed across all the possible orientations (**Figure 1c**).

ATR-FTIR analysis was used to identify BSA encapsulation within the fibres (**Figure 2a**). To address the issue of sensitivity in this method, 50% BSA was employed in relation to the polymer mass for the analysis. In the PCL spectrum, methylene groups were detected at  $2944$  and  $2867$   $\text{cm}^{-1}$ , and the band at  $1725$   $\text{cm}^{-1}$  indicated the presence of a carbonyl group. The in-plane bending of the carboxylic acid appeared at  $1472$   $\text{cm}^{-1}$ , while the out-of-plane bending was seen at  $959$   $\text{cm}^{-1}$ . Between  $1300$  and  $1000$   $\text{cm}^{-1}$ , carbon-oxygen bond stretching was observed. A distinctive band at  $731$   $\text{cm}^{-1}$  was attributed to the scissor-like bending vibration of methylene groups.<sup>[28]</sup> The interaction between BSA protein and PCL was monitored by analysing the spectral changes. Peaks between  $1645$  and  $1525$   $\text{cm}^{-1}$  correspond to the vibration modes of the amide I and amide II groups in the BSA molecule,<sup>[29]</sup> clearly indicating successful integration of BSA in the PCL fibres. Many peaks associated with the PCL structure, such as those for C—O, C—O—C, and C=O groups, exhibited shifts and reduced intensity, suggesting the formation of secondary interactions, such as hydrogen bonding, between the polymer and BSA. Further evidence of BSA incorporation into the PCL fibres was provided by the appearance of polar functional groups linked to BSA, along with increased hydrophilicity of the biohybrid fibres (**Figure 2b**). In the FA:AA system, the contact angle decreased significantly by 9% with the incorporation of BSA. In the AA solution, BSA incorporation reduced the contact angle of the produced fibres by 5%.

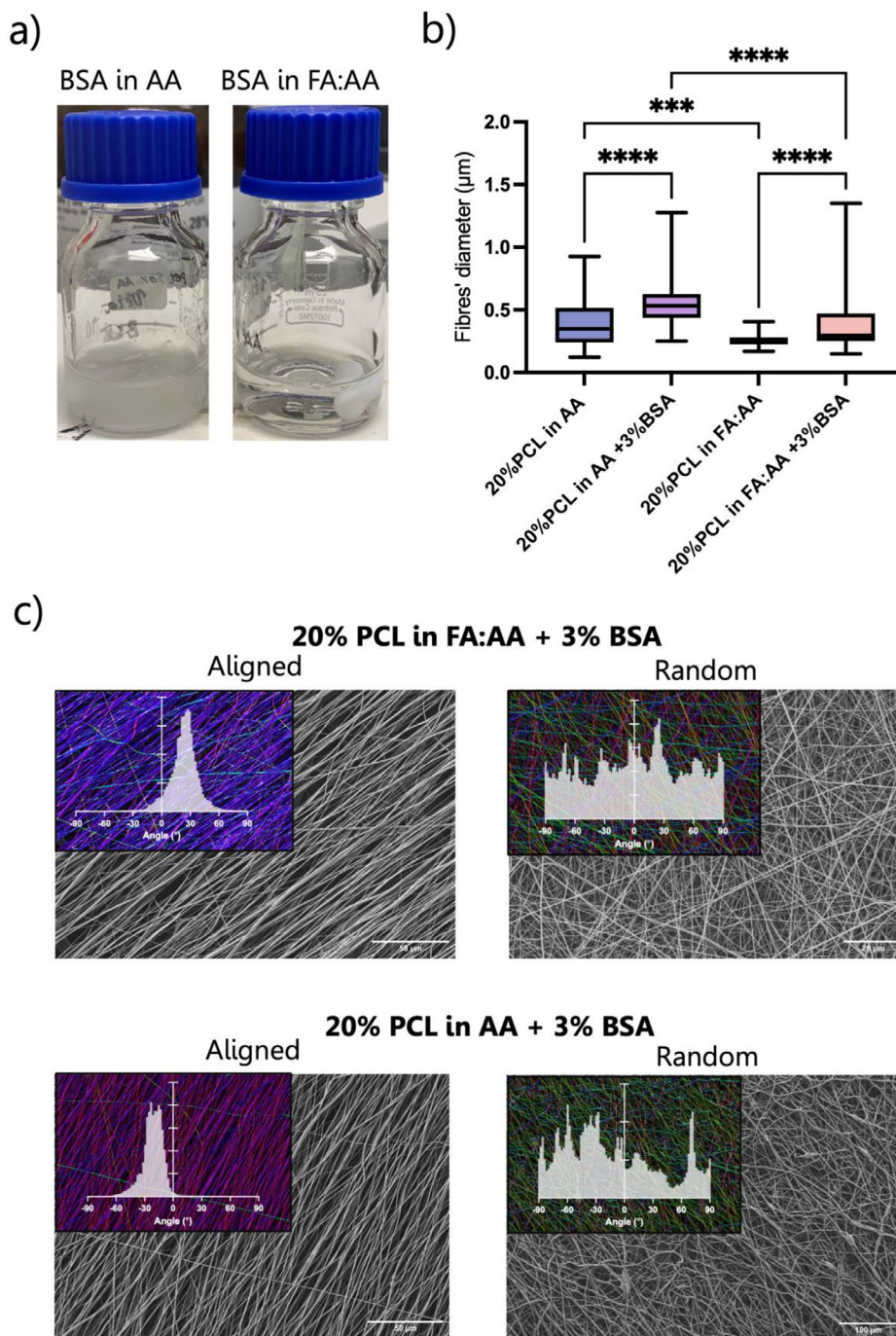


**Figure 1.** Morphological analysis of the fibres. a) Visible differences in BSA solubility in AA and FA:AA solvent systems. b) Fibre diameter of electrospun fibres from both solvent systems, with and without the addition of BSA. c) SEM images and directionality analysis of electrospun PCL fibres from both solvent systems, with and without BSA. Statistical analysis was performed with one-way ANOVA followed by Kruskal–Wallis multiple comparisons test with \*  $p < 0.05$ , \*\*  $p < 0.01$ , \*\*\*  $p < 0.001$ , \*\*\*\*  $p < 0.0001$ .

ATR-FTIR was used to investigate the secondary structure and conformational changes of BSA induced during the preparation of the electrospun fibre mat (Figure 3). Protein integrity is commonly evaluated by the study of the amide I band ( $1700\text{--}1600\text{ cm}^{-1}$ )<sup>[29]</sup> and the amide II band ( $1540\text{ cm}^{-1}$ ). The peaks between  $1650$  and  $1655\text{ cm}^{-1}$  are characteristic of  $\alpha$ -helical

structure; peaks ranging from  $1610\text{--}1620\text{ cm}^{-1}$  represent  $\beta$  sheet; and peaks from  $1660$  to  $1670\text{ cm}^{-1}$  and  $1680\text{--}1690\text{ cm}^{-1}$  are assigned to  $\beta$ -turns.<sup>[30]</sup>

The second derivative method was employed for band deconvolution to identify the number and positions of bands within the amide envelopes.<sup>[31]</sup> The amide I band was deconvoluted using

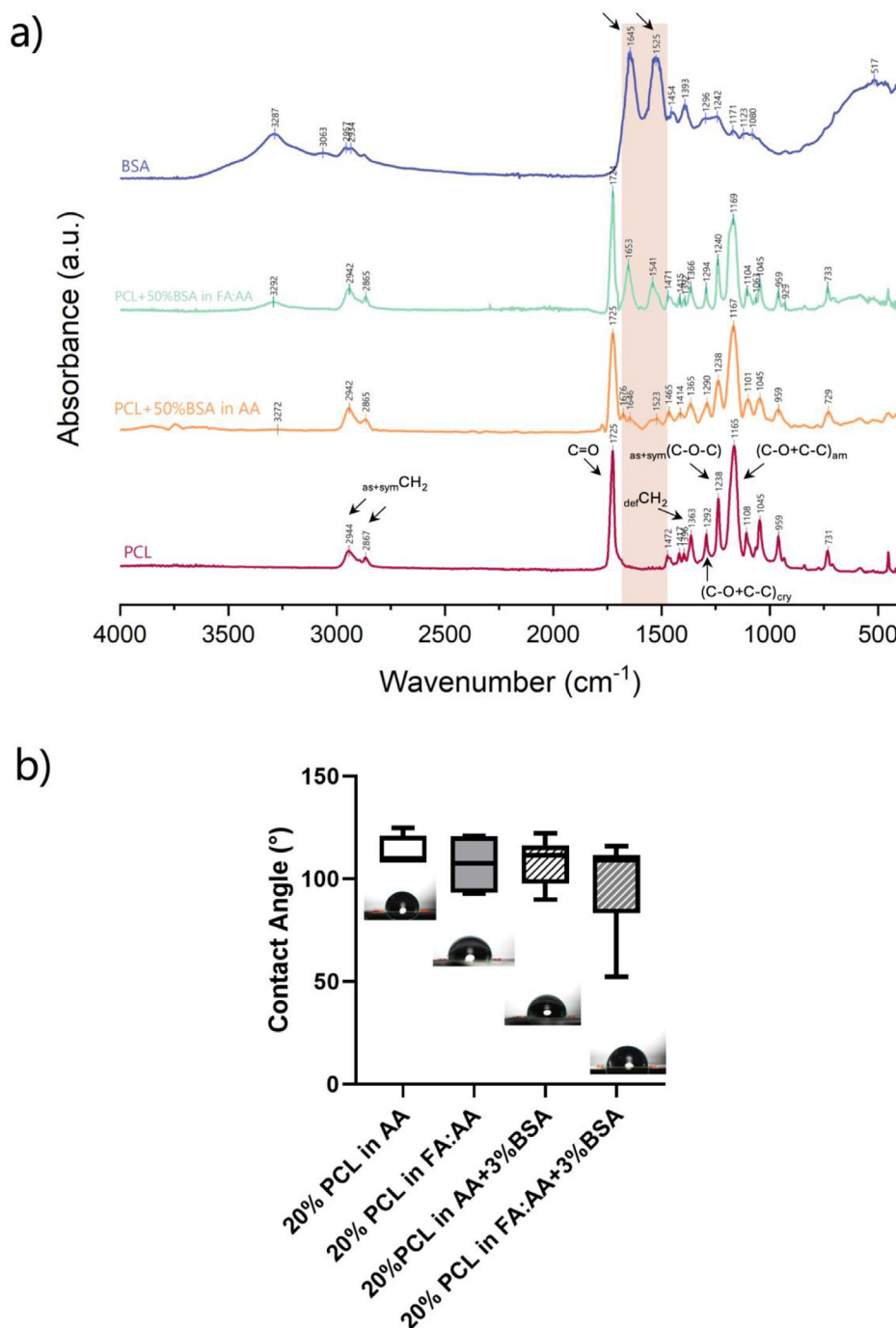


**Figure 2.** FTIR Spectra and contact angle analysis of BSA-loaded fibres. a) FTIR spectra of lyophilized BSA compared with BSA-loaded fibres fabricated from 20% PCL using AA and FA:AA solvent systems, with a BSA-to-polymer mass ratio of 50%. b) Water contact angle measurement for the fibre mats before and after BSA encapsulation.

a Gaussian line function, with the component positions identified based on the second derivative of ATR-FTIR spectra obtained from lyophilized BSA and fibres containing 50% BSA. The percentage of each component was calculated according to the corresponding integrated area.

Peak areas assigned to secondary structure elements revealed that lyophilised BSA contained  $35 \pm 4\%$

$\alpha$ -helix,  $34 \pm 4\%$   $\beta$ -sheet,  $27 \pm 4\%$   $\beta$ -turn, suggesting that the secondary structures of BSA were dominated prevalently by  $\alpha$ -helix conformation and  $\beta$ -sheet (Figure 3a,b). Lyophilised BSA and BSA in polymer solution demonstrated conformational changes when adsorbed on material surfaces. Spectra obtained from AA polymeric fibres loaded with BSA showed a reduction of the  $\alpha$ -helix content to  $15 \pm 1\%$ ,  $5 \pm 0\%$   $\beta$ -sheet and  $19 \pm 1\%$



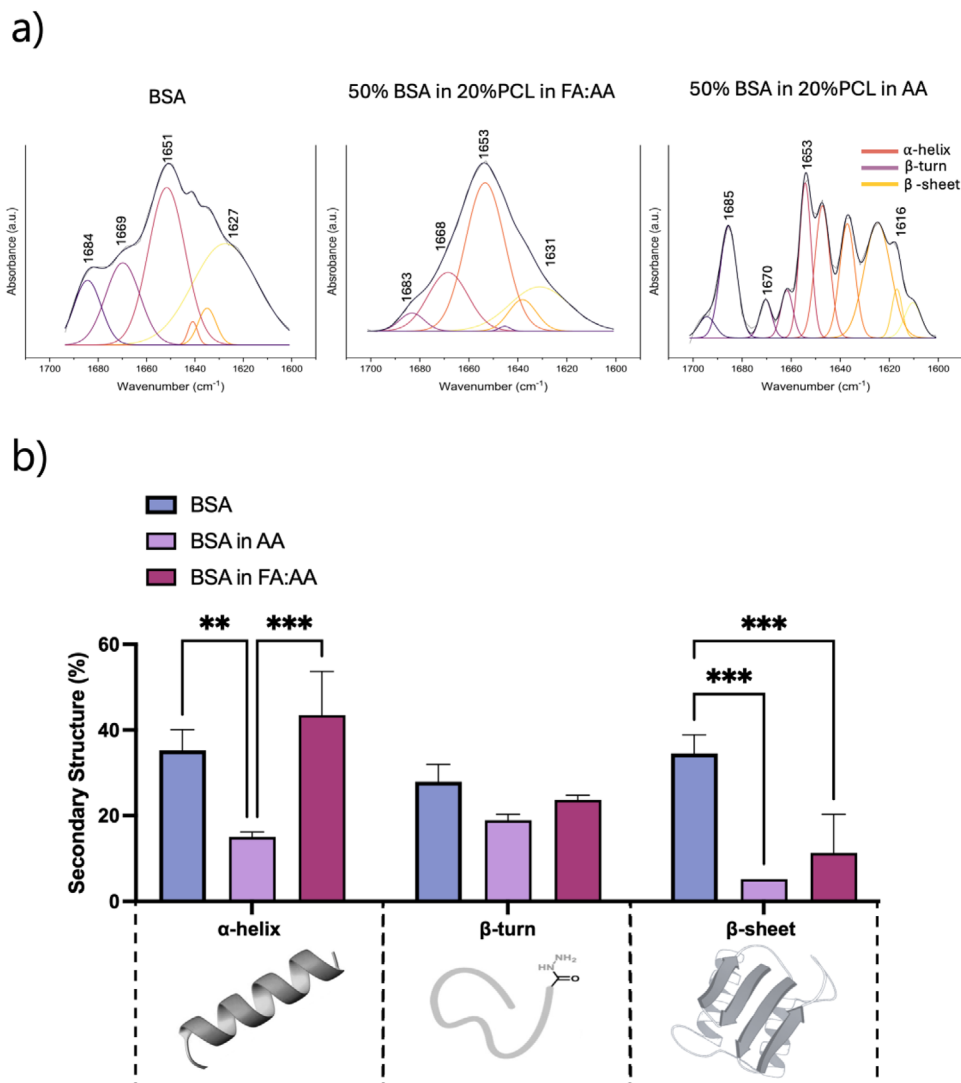


**Figure 3.** Deconvolution of Amide I absorption band of BSA lyophilized and in the two electrospun solutions made by 20%PCL, 50%wt. BSA and AA and FA:AA. a) Gaussian deconvolution of the Amide I FTIR spectra between 1600 and 1700  $\text{cm}^{-1}$  showed different relative amounts of the three main features involved in the BSA structure. b) Relative contribution of protein secondary structure features in BSA within the polymeric fibrous mats obtained in different solvent systems. Statistical analysis was performed with two-way ANOVA followed by Tukey's multiple comparisons test with \* $p < 0.05$ , \*\* $p < 0.01$ , \*\*\* $p < 0.001$ , \*\*\*\* $p < 0.0001$ .

$\beta$ -turn structures. Conversely, in the FA:AA polymer solution the BSA tertiary structure changed but the  $\alpha$ -helix amount was higher with  $43 \pm 5\%$   $\alpha$ -helix,  $11 \pm 8\%$   $\beta$ -sheet and  $23 \pm 1\%$   $\beta$ -turn structures. As previously demonstrated,<sup>[31]</sup> the tertiary structure of BSA is predominantly constituted by  $\alpha$ -helix structure. This structure was best maintained in the FA-containing polymer solution suggesting not only better BSA compatibility with the solvent.

## 2.2. Mesoporous Silica Particles Successfully Incorporate BSA

BSA encapsulation efficiency and loading capacity were evaluated to optimize the processing parameters for MSN synthesis. The highest protein encapsulation efficiency was achieved in silica

particles synthesized using 6 mL of TEOS with a reaction time of 4 h (S1, Supporting Information).

The  $\text{N}_2$  adsorption/desorption isotherms for  $\text{SiO}_2$  samples and BSA-loaded particles were determined (Figure 4). Based on the IUPAC classification, the obtained isotherms for all samples are of type IV, hence characteristic of mesoporous materials.<sup>[32,33]</sup> In the simple mesoporous silica particles (Figure 4a), we observed very little hysteresis, as a consequence of the adsorption and desorption of empty pores. Conversely, in the BSA-loaded samples, the isotherm curve was characterized by an H2 hysteresis due to pore-blocking/percolation effects induced by the protein molecules (Figure 4b). Pore size distribution was determined by the BJH model.<sup>[33]</sup> The surface area of the mesoporous nanoparticles was observed to be  $774 \text{ m}^2 \text{ g}^{-1}$ . Upon loading with BSA, a reduction in surface area was

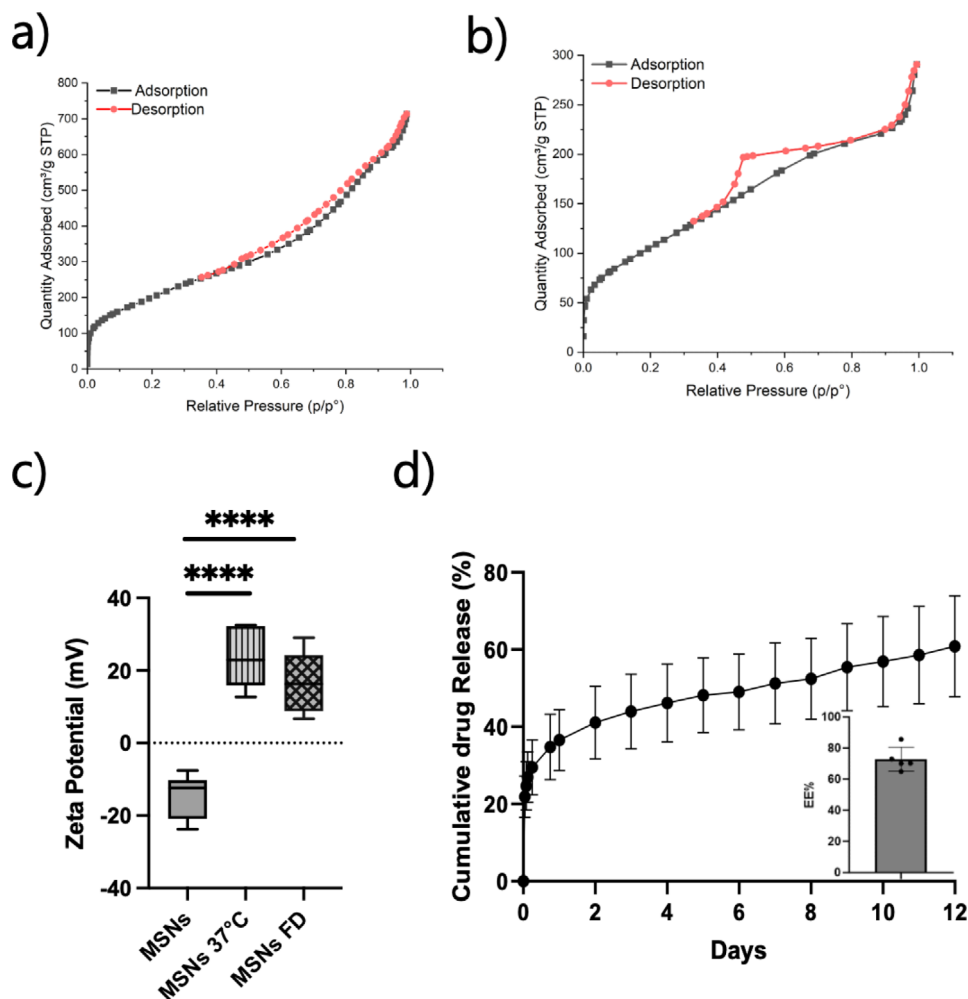


**Figure 4.** MSNs porosity, Zeta Potential and BSA release from MSNs. Nitrogen adsorption and desorption isotherms and pore size distribution of MSNs, before a) and after b) BSA adsorption. c) Zeta potential measured before and after the encapsulation of BSA in the particles. d) BSA cumulative release from MSNs (inset: BSA encapsulation efficiency) Statistical analysis was performed with ordinary one-way ANOVA. \* $p < 0.05$ , \*\* $p < 0.01$ , \*\*\* $p < 0.001$ , \*\*\*\* $p < 0.0001$ .

observed to  $401 \text{ m}^2 \text{ g}^{-1}$ , indicating protein adsorption on the particles.

The isoelectric point (pI) of BSA was previously determined as pH 4.64 indicating a net positive charge below the pI value and a net negative charge above the pI value;<sup>[34]</sup> MSNs had a pI of 3.64. Zeta potential at pH 7 indicated a change from negative to positive for MSNs following BSA encapsulation (Figure 4c). Finally, BSA release from MSNs was analysed across a period of 12 days (Figure 4d). The drug release kinetic is described in two phases; an initial burst release during the first 3 h, followed by a slow release of the remaining BSA. In the burst release phase,  $\approx 24\%$  of BSA was released, and by day 12 we observed 60% release.

### 2.3. Lysozyme and GDF-7 are Efficiently Encapsulated in Mesoporous Silica Nanoparticles

Lysozyme and GDF-7 have pI's equal to 10.7<sup>[35]</sup> and 9,<sup>[36]</sup> respectively, resulting in both proteins having a net positive charge at

pH 7, in contrast to the net negative charge of MSNs. As a result, there is a strong electrostatic attraction between the MSNs and proteins, and correspondingly high encapsulation efficiencies, at 98.5% for lysozyme and 99.9% for GDF-7. Under release conditions, lysozyme had a minimal burst release phase, followed by sustained linear release. Across 70 days we observed 16% of the drug released, equivalent to a cumulative amount of  $63 \pm 5 \mu\text{g}$  (Figure 5a). GDF-7's behaviour was predicted to be similar, but possibly due to only a portion of the media being removed at each time point, residual GDF-7 in the released media had slower diffusion. After 5 days only 0.04% was released, equivalent to  $7.6 \pm 1 \text{ ng}$  (Figure 5b).

The controlled release of the lysozyme was modelled by the first-order kinetic ( $R^2 = 0.9806$ ) (Table 1). Following the prediction rules of this model, this means that the amount of release of the active molecule, entrapped in the solid porous structure, is proportional to the amount of remaining drug in the matrix.<sup>[37,38]</sup> Thus, the amount of lysozyme released tends to decrease in function of the time.

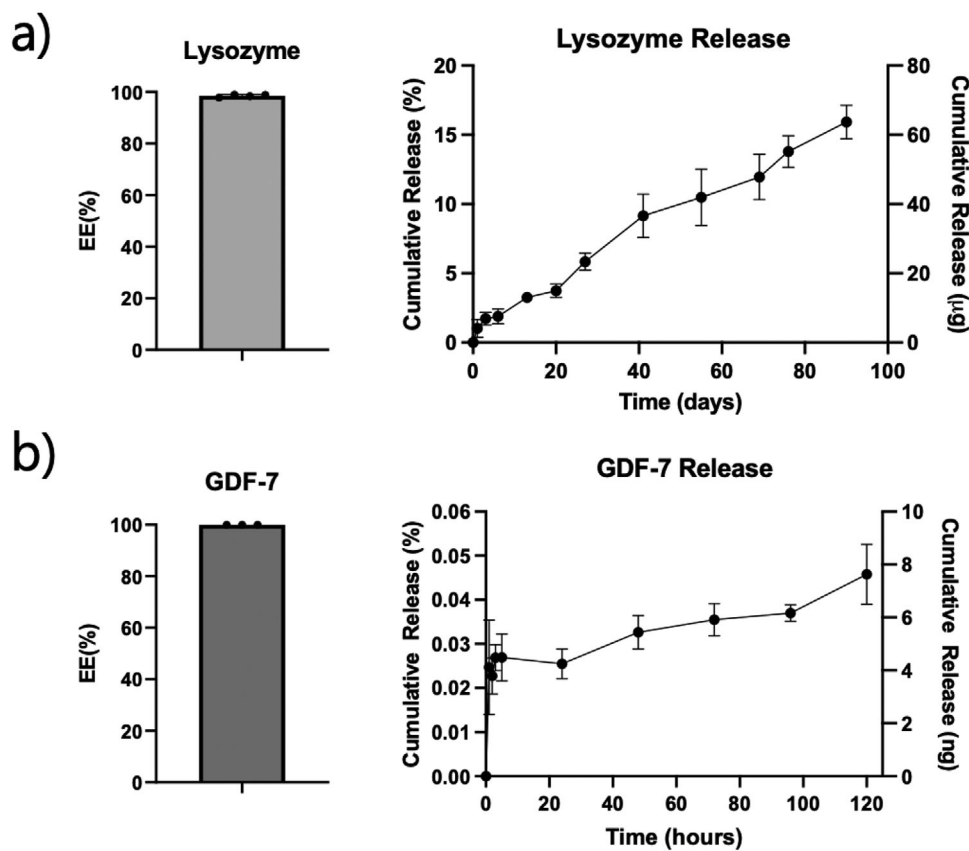


**Figure 5.** Encapsulation and release of lysozyme and GDF-7 from MSNs. a) Lysozyme's EE and release profile from MSNs b) GDF-7's EE and release profile from MSNs.

#### 2.4. Mesoporous Silica Nanoparticles Protect Drugs from Both Solvents and Electrospinning Process Parameters

Aligned fibres with MSNs were characterized. Fibre diameter was  $342 \pm 90$  nm from PCL:AA:MSN suspensions and  $141 \pm 30$  nm from PCL:FA:AA:MSN suspensions. In AA, MSNs were channelled within the PCL fibres during production, while in FA:AA, the particles moved to the surface and clustered together (Figure 6a,b). The MSN distribution was further confirmed by EDS mapping (Figure 6c,d). The EDS elemental maps for carbon (C), oxygen (O), and silicon (Si) confirm the presence of MSNs in both fibre types. Gold (Au), originating from the coating applied for image acquisition, has not been displayed as it is not relevant to the analysis. In the fibres electrospun using AA as solvent (left panel), the Si signal was homogeneously distributed throughout the fibre network, indicating successful MSN incorporation within the polymer matrix. In contrast, fibres fabricated using a FA:AA solvent mixture (right panel) exhibited pro-

nounced MSN clustering, with Si-rich aggregates localized outside the fibre structure.

We compared the ATR-FTIR profiles of PCL fibres, pure BSA, pure MSNs and the BSA-loaded MSNs embedded in PCL fibres. Compared to the pure PCL fibres, the samples with incorporated BSA-loaded MSNs presented two new peaks at  $1654$  and  $1542$   $\text{cm}^{-1}$  induced by the presence of BSA (peaks at  $1645$  and  $1533$   $\text{cm}^{-1}$ ). The other two peaks, not present in the PCL sample, are at  $1065$  and  $1107$   $\text{cm}^{-1}$ , and overlap with the BSA-loaded MSNs peaks. Finally, a peak at  $453$   $\text{cm}^{-1}$ , was detected in the MSNs-loaded fibres, due to the overlapping peaks of both BSA ( $520$   $\text{cm}^{-1}$ ) and BSA-loaded MSNs ( $449$   $\text{cm}^{-1}$ ) (Figure 7). These new peaks were accentuated in the FA:AA sample, and we hypothesize that this could be due to the higher exposure of the particles on the surface of the fibres compared to the sample in AA, in which the particles are more uniformly distributed along the thickness of the polymer structure.

**Table 1.** Regression coefficient ( $R^2$ ) of four different kinetic models fitted to the lysozyme release from MSNs.

Model	Korsmeyer-Peppas ( $R^2$ )	n	Zero-Order ( $R^2$ )	First-Order ( $R^2$ )	Higuchi ( $R^2$ )
Sample					
Lysozyme-loaded MSNs	0.9448	0.66	0.9792	0.9806	0.9049

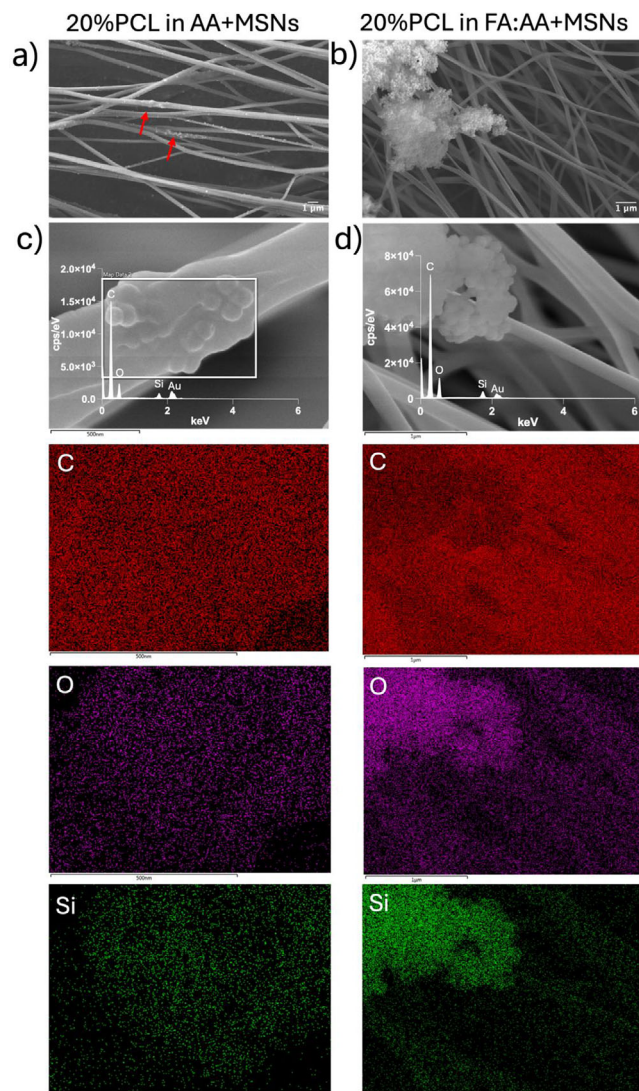


**Figure 6.** SEM/EDS characterization of BSA-loaded MSNs embedded in PCL-aligned fibres. SEM image analysis show the distribution of particles inside the fibres produced in AA a) and in FA:AA b). Panels c) and d) display EDS maps of fibres produced from AA and FA:AA, respectively, highlighting the presence of C (polymer component), Si, and O (originating from the MSNs).

Lysozyme was utilised as a model protein to determine retained enzymatic activity following the electrospinning procedure. ATR-FTIR spectra were analysed to evaluate conformational changes in lysozyme following its direct incorporation into the polymeric solution prepared in acetic acid. Specifically, the Amide I band was deconvoluted using a Gaussian line function, with component positions identified from the second derivative of ATR-FTIR spectra obtained from lyophilized lysozyme and fibres containing 50% lysozyme (Figure 8a). As with BSA, conformational changes were observed, evidenced by a redistribution in the relative contributions of the three primary structures:  $\alpha$ -helix,  $\beta$ -turns, and  $\beta$ -sheets.

The release of lysozyme from MSNs embedded in 20% PCL fibres (AA) showed a slow and steady behaviour, reaching 100% re-

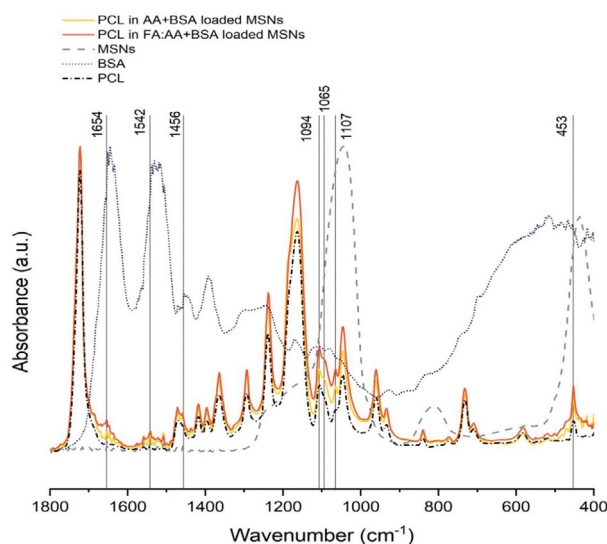


**Figure 7.** FTIR characterization of BSA-loaded MSNs embedded in PCL-aligned fibres. FTIR spectra in the Amide I and Amide II regions of BSA, PCL, MSNs and fibrous mat composite formed from their combination.

lease after 23 days (Figure 8b). Lysozyme released during the initial 6 days exhibited reduced enzymatic activity, while at later time points, a substantial improvement in enzymatic activity was observed, culminating in a final activity level  $\approx 12$ -fold higher than at the initial time point (Figure 8c). The lysozyme used had an activity of  $\geq 20\,000\text{ U mg}^{-1}$ , enabling the estimation of a predicted activity based on the amount of drug released. The initial predicted activity was recorded as  $134 \pm 13\text{ u mL}^{-1}$ ; however, post-electrospinning, a decrease of 133 units was observed. By the endpoint of this study, the difference between the predicted and experimentally measured activity was  $\approx 27$  units (Figure 8d).

The release profiles of lysozyme-loaded MSNs, initially characterized by first-order kinetics, transitioned to Korsmeyer-Peppas kinetics upon embedding the MSNs into the polymeric scaffold. With an  $n$ -value  $< 0.45$ , the drug transport mechanism is classified as non-Fickian, indicating that release is influenced by both diffusion and swelling processes.

## 2.5. The Particle-Fibre Composite as a Mechanical Supportive Scaffold for the Attachment and Proliferation of MSCs

Ensuring that the mechanical characteristics of fibres align with the demands of a particular end-use is crucial. Mechanical tests were performed on fibres with and without the incorporation of MSNs. Figure 9a shows how the samples were prepared for the mechanical test. Length and width were calculated by imaging analysis. To generate the stress-strain curve fibres were pulled until rupture at a rate of  $5\text{ mm min}^{-1}$  and with a pretension of  $0.02\text{ N}$  (Figure 9b). The mechanical properties of the fibres displayed a non-linear behaviour. For strains up to 3%, so in the small strain region, the stress-strain relationship is not linear (exponential increase).

The Young's Modulus of fibres from AA was  $53 \pm 3\text{ MPa}$ , 52% higher than that measured on fibres obtained using FA:AA (equal to  $26 \pm 2\text{ MPa}$ ). The direct incorporation of BSA resulted



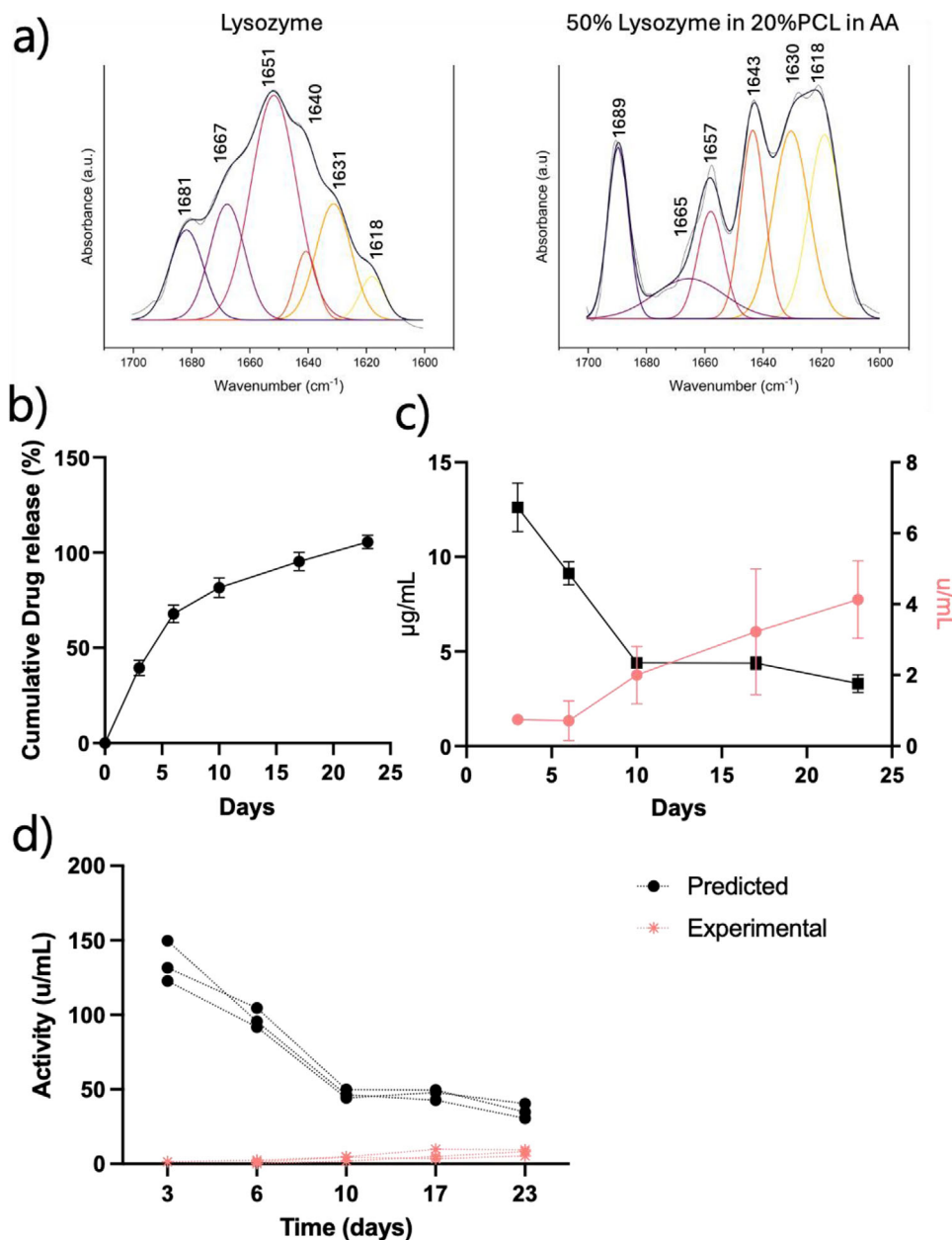


**Figure 8.** Lysozyme release from MSNs embedded in 20%PCL aligned fibres. a) Gaussian deconvolution of the Amide I FTIR spectra between 1600 and 1700  $\text{cm}^{-1}$  showed a different relative amount between the three main structures involved after lysozyme direct blending into 20%PCL fibres made in AA. b) Release profile of lysozyme from lysozyme-loaded MSNs embedded within electrospun fibres. The graph depicts the cumulative release percentage of lysozyme over time, measured in days. Lysozyme was completely released after 23 days. c) The activity analysis revealed that lysozyme exhibited low activity at the initial two-time points, followed by a gradual increase over time. d) Comparison between predicted and experimental activity.

in a reduction of the mechanical properties of fibres produced in AA, as evidenced by a Young's Modulus of  $25 \pm 10$  MPa. In contrast, the FA:AA formulation exhibited an 84% increase in Young's Modulus ( $48 \pm 12$  MPa), compared to the BSA-free counterpart. The presence of MSNs led to a decrease in mechanical properties in both scenarios, with values of  $18 \pm 7$  MPa and  $22 \pm 5$  MPa recorded for fibres produced in AA and FA:AA, respectively (Figure 9c).

In AA, fibres displayed the greatest strain at the point of breaking ( $0.99 \text{ mm mm}^{-1}$ ), resulting in the highest level of resilience. Following BSA integration, the percentage decreased to  $0.53 \text{ mm mm}^{-1}$  and after the integration of MSNs,  $0.65 \text{ mm mm}^{-1}$ . There were no notable disparities noted between BSA and MSN-loaded fibres. The fibres in FA:AA were found to be generally more brittle and fractured with little deformation. A slight enhancement in performance was seen following BSA

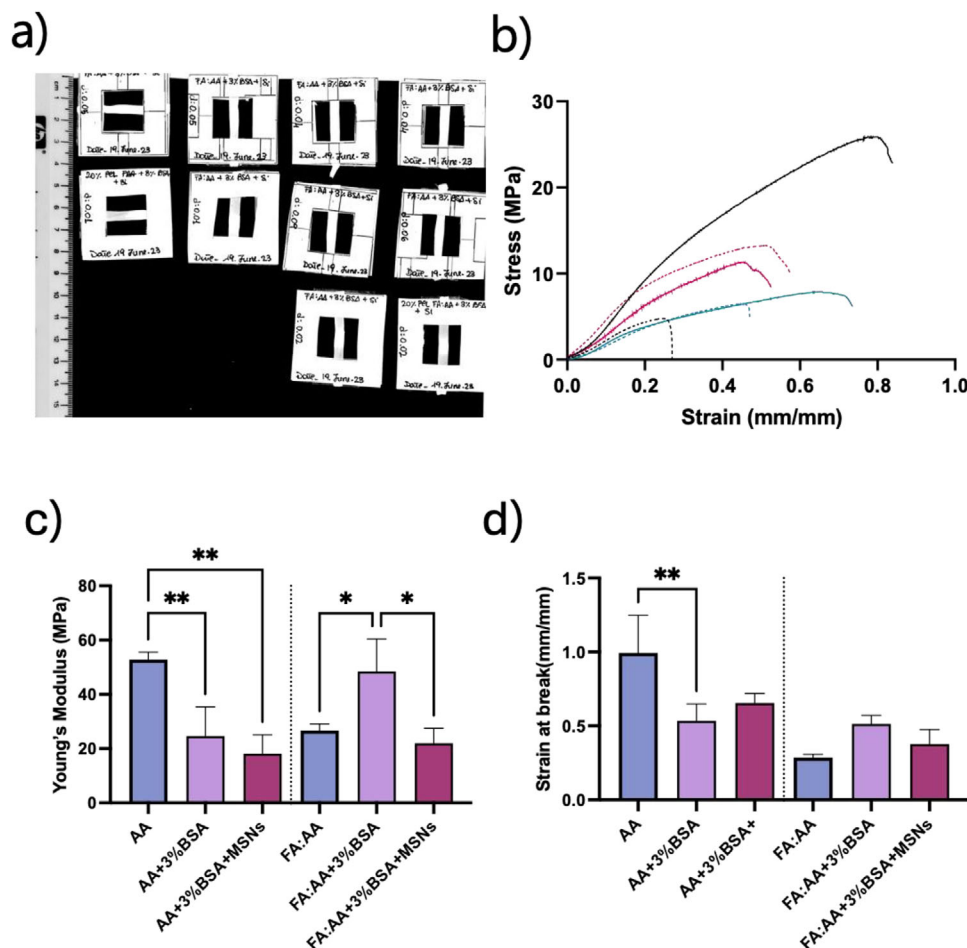


**Figure 9.** Mechanical analysis. a) Example of the sample preparation used to measure the exact geometrical parameters for the conversion of the measured force-displacement curve in stress-strain curves. b) Typical stress/strain graphs of the various fibre compositions. The colors black, pink, and blue represent the 20%PCL fibres, the fibres loaded with BSA, and the BSA-loaded MSNs incorporated in the fibres, respectively. Solid lines represented fibres from AA while dotted lines represented fibres from FA:AA. c) Elastic modulus obtained as slope of the linear region of the stress-strain curves. d) Strain at break, defined as the strain at which the samples experience breakage. The porosity of fibres electrospun using AA was measured at 90%, while those electrospun using a mixture of FA:AA exhibited a porosity of 86%. Statistical analysis was performed with ordinary one-way ANOVA followed by Tukey's multiple comparisons test with \* $p < 0.05$ , \*\* $p < 0.01$ , \*\*\* $p < 0.001$ , \*\*\*\* $p < 0.0001$ .

encapsulation, showing a strain at a break of  $0.51 \text{ mm mm}^{-1}$ , but no noticeable distinctions were found between the BSA-free, BSA and MSNs groups (Figure 9d).

## 2.6. Aligned PCL Fibres Incorporating MSNs Provide 3D Structures for Cell Attachment, Proliferation, and Migration

To assess cell attachment and viability on the fibres we undertook an investigation using both MSCs and TSCs type II, a multipotent tendon progenitor cell.<sup>[39]</sup> We focussed this section of our study on fibres made from 20% PCL in AA scaffold with the incorporation of MSNs. This selection is grounded in the demonstrated capability of these types of scaffolds to better incorporate the MSNs intended as carriers for future soluble signals, including GDF-7.

Scaffolds were mounted on polylactic acid (PLA) 3D printed rings (Figure 10a) and underwent plasma treat-

ment as a functionalization step. This process led to heightened hydrophilicity of the scaffold, as evidenced by a significant reduction in the contact angle to  $14.45^\circ$  compared to the untreated sample contact angle of  $123.46^\circ$  (Figure 10b).

Cell metabolic activity was determined by Alamar blue analysis. Over a period of 21 days, total cell metabolic activity increased, and was consistently higher in 2% oxygen condition compared to 21%, in both cell types (Figure 10c). Cell viability assessment using confocal imaging of live/dead assay (Figure 10d) demonstrated that green-stained live cells increased, for both MSCs and TSCs, over time. Red staining was detected solely around agglomerates of particles, leading us to believe it was adsorbed by the particles, and that no dead cells were stained. Scaffold orientation guided cells to align in the direction of the fibres. In MSCs cultures, this event occurred from the initial time points, while in TSCs cultures, the first noticeable alignment was only seen by day 14. Higher confluency was observed in both cell types cultured in

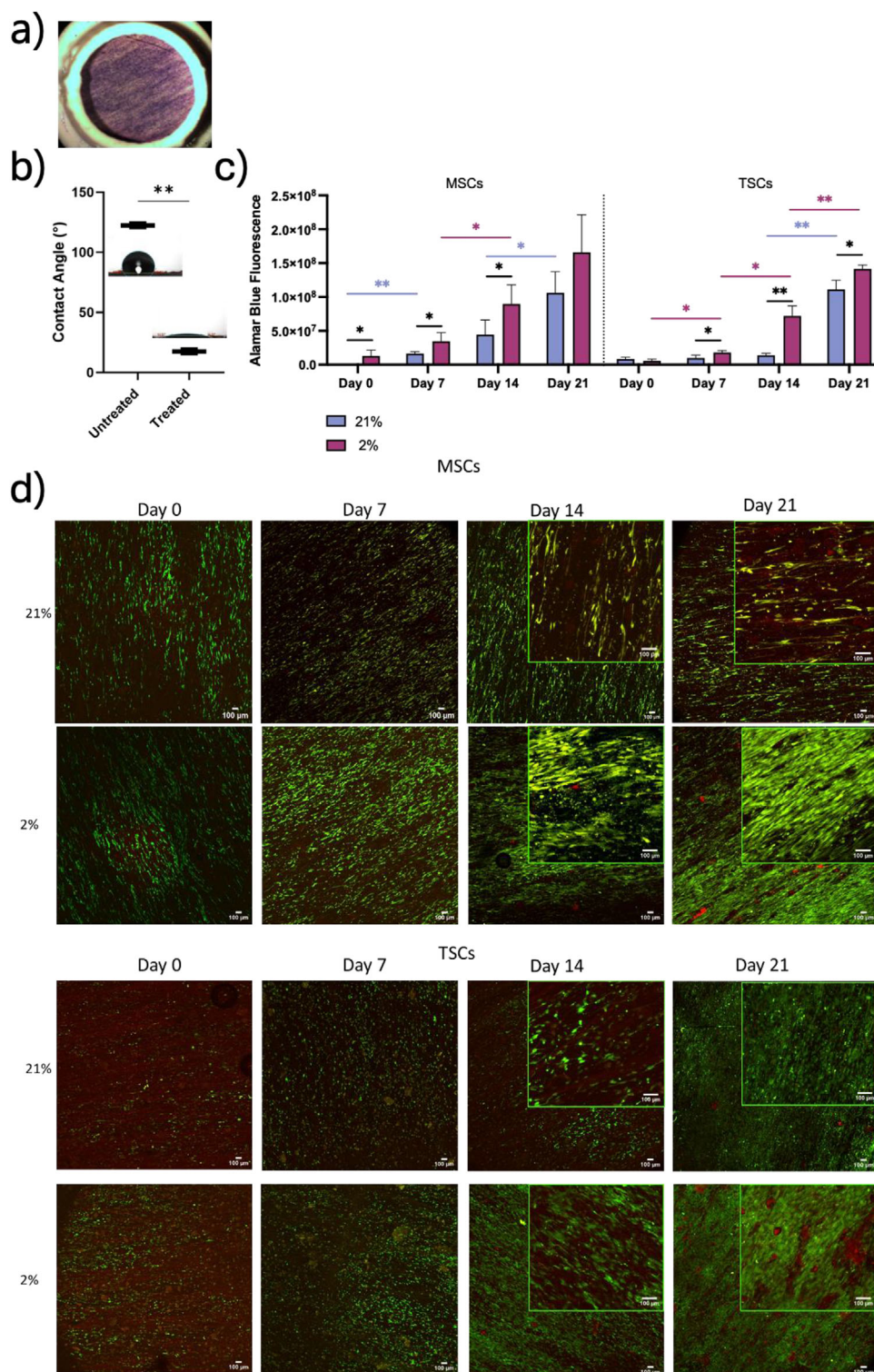


**Figure 10.** Cell attachment and proliferation. a) Custom-made fibre mesh support, made in 3D printed PLA and melt-adhered onto the fibre mat. b) Contact angle measurement before and after plasma treatment. c) Alamar Blue metabolic activity assay over a period of 21 days. d) Live/dead assay performed on MSCs and TSCs on fibre scaffolds. Scale bars are 100 μm. Statistical analysis was performed with RM two-way ANOVA test with \* $p < 0.05$ , \*\* $p < 0.01$ , \*\*\* $p < 0.001$ , \*\*\*\* $p < 0.0001$ .

2% oxygen concentration, compared to 21%, in accordance with data obtained by the Alamar blue analysis.

### 3. Discussion

Tissues and organs often feature hierarchical layered structures with specific ECM compositions and anisotropic properties, which deliver distinct signals to cells and provide the tissue with the mechanical properties needed for physiological functions. Electrospinning, among other scaffold fabrication techniques, allows the bottom-up assembly of layered nanofibre/cell constructs, and the inclusion of growth factors can be a valuable approach for regulating cell behaviour. In this way, the combination of the hierarchical organization of nanofibres with the integration of various bioactive molecules can be an efficient approach to support functional tissue formation. In this research, we found substantial alteration of encapsulated protein structure during electrospinning and suggested using an intermediate carrier, like MSNs, to shield the biomolecules during this process while also creating a surface that promotes cell alignment. This approach produced a biocompatible scaffold for tendon tissue engineering and partially mitigated electrospinning-induced structural changes to encapsulated biomolecules.

Incorporation of proteins into electrospun fibres must overcome the challenge that most proteins undergo denaturation during electrospinning due to the strong electric field and the presence of organic solvent.<sup>[40]</sup> However, some proteins withstand both denaturation factors and retain their functionality after electrospinning. These proteins include insulin,<sup>[41]</sup> chymotrypsin<sup>[42]</sup> and others.<sup>[43]</sup> In our study we initially used BSA as a protein model. In the solution obtained in FA:AA, we observed a higher solubility of the protein, consistent with the work of Houen et al.<sup>[44]</sup> who showed that AA was almost ineffective in dissolving BSA, compared to FA where the solubility reached values of 50 mg mL<sup>-1</sup>. The observed behaviour can be explained by differences in dielectric constants and hydrogen bonding properties of the solvents.<sup>[44]</sup> Indeed, the BSA solution obtained in FA:AA was more transparent, indicating better compatibility with BSA. Infrared spectroscopy was used to assess the secondary structure of BSA. BSA has a significant level of  $\alpha$ -helix content at pH 7, evident in a prominent peak at 1657 cm<sup>-1</sup>, along with other bands indicating  $\beta$ -sheet structures (1691, 1640, and 1631 cm<sup>-1</sup>), turn (1681 cm<sup>-1</sup>), and random coil (1650 cm<sup>-1</sup>).<sup>[45]</sup> After the electrospinning procedure, the band deconvolution of the BSA-loaded fibres revealed a different distribution of the three main structures recognized as responsible of the protein tridimensionality, with respect to the lyophilized BSA spectrum. The fibres obtained in AA, showed a dramatic reduction in the  $\alpha$ -helical content; it has previously been demonstrated that degradation of BSA quickly occurs during incubation in acidic solutions, resulting in significant loss of its original tertiary structure.<sup>[46]</sup> This likely happens because the ionizable protein groups (pKa > 3) are protonated, and charge repulsion drives the unfolding of the molecule. Past research on BSA trapped in PLGA delivery systems showed incomplete release patterns. Analysis of the protein still trapped in the PLGA indicated noncovalent aggregation and peptide bond fragmentation, suggesting exposure to a very acidic environment.<sup>[47]</sup>

Drug delivery systems have benefited from the advancements in nanomaterials,<sup>[48,49]</sup> particularly MSNs, which provide a large surface area, significant pore volumes, customizable pore sizes, and the capability to protect encapsulated drugs and proteins.<sup>[50–53]</sup> MSNs can be integrated into polymer fibres to form composite materials with benefits including sustained release and protected bioactivity of the encapsulated drugs.<sup>[54]</sup>

In accordance with the IUPAC categorization, the isotherms depicted for MSN samples are classified as type IV,<sup>[55]</sup> thus possessing the typical properties of mesoporous materials. At lower relative pressure, a monolayer and subsequent multi-layer adsorption occurs on the external surface and on the pore walls. As the relative pressure increases an increase in the adsorption volume occurs due to pores being filled with adsorbate through condensation whereby the gaseous adsorbate condenses into the pores in its liquid state.<sup>[32]</sup> The most characteristic feature of type IV isotherms is the plateau at higher relative pressures, which occurs when saturation is approached. Its length is variable and depends on the pore size: the presence of this plateau confirms that the pores are sufficiently small to be fully occupied by the adsorbate. In our case, the second region of adsorption occurs at higher relative pressure, and it increases asymptotically to the volume axis. This is indicative of an incomplete filling of the pores.<sup>[33]</sup> Capillary condensation is commonly associated with hysteresis, which can be observed in both individual pores and pore networks. Hysteresis is typically considered in three contexts: within individual pores, due to pore network connectivity, and in disordered or inhomogeneous materials, where both kinetic and thermodynamic effects across the entire pore system are involved.<sup>[56]</sup> In the BSA-free mesoporous silica particles, we observed very little hysteresis. This could be due to close-ended pores: the adsorbed monolayer is present on the walls but also on the base of the pore. Condensation commences at the base of the pore, and the pore will be filled by the formation of a meniscus across the pore, and the process continues until the pore is completely filled with the adsorbate.<sup>[57]</sup> With this pore geometry, the adsorption and desorption processes are quite similar, so we can expect little hysteresis between the isotherms. In the BSA encapsulated samples, we observed an H2 hysteresis due to pore blocking/percolation effects induced by the protein's molecules.<sup>[57]</sup> H2 isotherms are associated with pores structures that have an internal restriction, represented in this case by the BSA protein. When MSNs are loaded with BSA, the protein molecules can partially occlude the pore entrances, effectively acting as a blocking agent. This occlusion alters the accessible pore geometry and connectivity, leading to modified capillary condensation and evaporation dynamics. As a result, during gas desorption, the restricted pore network exhibits a delayed release of adsorbed molecules, characteristic of a type H2 hysteresis loop.<sup>[58]</sup> This type of isotherm is typically associated with “ink-bottle” pores, where narrow necks hinder the desorption process; the presence of such constrictions delays the desorption of adsorbate until a threshold is reached, leading to a steep desorption branch.<sup>[58]</sup>

At a pH defining their isoelectric point, proteins have a net neutral charge, at a pH below the pI they have a net positive charge, and conversely a negative charge above this. BSA's pI has been determined as pH 4.64<sup>34</sup> and the MSNs as pH 3.64. BSA encapsulation and zeta potential analysis were performed around pH 7; consequently, both the protein and the MSNs will



carry a net positive charge resulting in an electrostatic repulsion between the protein and the particles. In our work, significant BSA immobilization still occurred at pH 7, suggesting that electrostatic interaction is not the only mechanism of BSA adsorption. Given the proteins' size and the high number of functional groups, additional types of interactions have been recognized as fundamental to protein-MSN interactions,<sup>[59,60]</sup> including protein structure conformation. In particular, the hydrodynamic size of protein molecules depends on the solution pH, which can also have a significant impact on its adsorption in the mesopores, and in fact, at pH 7, BSA reached its minimum hydrodynamic diameter (2.23 nm), favouring the adsorption in the mesoporous structure. As for BSA hydrophobicity, Li et al.<sup>[61]</sup> reported that changes in the pH from neutral pH caused BSA to unfold, thus exposing more hydrophobic groups, indicating that a significant adsorption mechanism will be the attraction of the hydrophobic side chains of the amino acid residues on the BSA to the silanol groups on the MSNs surface.<sup>[62]</sup> The engagement of the hydrophobic BSA chains with the particles is further demonstrated by the zeta potential switch from negative to positive, before and after the BSA encapsulation. At pH 7 we observed a relatively low BSA encapsulation efficiency, compared to the other two analysed molecules, due to the opposite charge accumulating respectively on the protein and on the particles. At the same time, this condition can favour subsequent protein release. The fast initial release accounted for the fast diffusion of the BSA molecules physisorbed on the surface of the MSNs, as a result of the high concentration gradient at the particle interface with the bulk PBS solution. As the BSA started to accumulate in the supernatant the diffusion gradient decreased, slowing down the release rate.

All BMPs are basic proteins with isoelectric points between 7.7 and 9, GDF-7 (BMP12) has an isoelectric point of 9<sup>36</sup>. With a pI of 10.7,<sup>[35]</sup> lysozyme was selected as a relevant model of GDF-7. Due to the neutral pH during encapsulation, both lysozyme and GDF-7 molecules will have a positive charge. Therefore, the primary adsorption process is likely the electrostatic attraction between MSNs and protein molecules with opposite charges. In support of this, a high encapsulation efficiency was observed in both cases. During the release, likely due primarily to electrostatic attraction, a slow lysozyme release was observed: after 70 days, only 16% was released. The anticipated behaviour of GDF-7 was expected to be alike; however, because only a fraction of the released media was discarded at each time point during the release process, the presence of residual GDF-7 in the released media may have caused a further reduction in the release.

Similar to the observations with BSA, lysozyme also experienced structural alterations when in direct contact with the polymeric solution. Therefore, it was hypothesized that MSNs could serve as effective protective carriers for the drug during the electrospinning process. Particles encapsulating lysozyme were successfully incorporated in 20% PCL fibres in AA. The evaluation of lysozyme release and activity was conducted to determine if MSNs could be a promising method to prevent protein degradation during electrospinning.<sup>[25,26]</sup> Following a 25-day period, all the predicted encapsulated lysozyme had been released, with the noteworthy observation that lysozyme activity was lower in the earlier release phase, possibly due to the release of surface-absorbed drug but subsequently rose once the drug was diffusing from the innermost pores of the MSNs. A

study conducted by Kao et al.<sup>[63]</sup> showed that the proteins enclosed in the nanopores of MSN maintained secondary structure integrity to a certain extent and this is associated with the sizes of the pores. Moreover, lysozymes housed within nanochannels were protected from thermal denaturation, allowing them to retain their functionality.<sup>[63]</sup> MSNs are effective nanocarriers, offering drug protection and targeted delivery, while their encapsulation in PCL fibres and strong electrostatic interactions with the drug minimize premature release.<sup>[64]</sup> Other research studies have also supported this finding, showing that drug-loaded MSNs enclosed in electrospun fibre networks can release drugs in a controlled manner, protecting them from denaturation.<sup>[65,66]</sup>

The release of lysozyme from MSNs followed first-order kinetics, indicating that the process was primarily diffusion-driven, governed by the concentration gradient between the porous structure of the nanoparticles and the surrounding release medium. When lysozyme-loaded MSNs were incorporated into the polymeric fibrous scaffold, the release was initially dominated by diffusion for particles located at the polymer surface. However, for those embedded within the scaffold, the release became progressively constrained by the rate of lysozyme diffusion through the polymeric matrix. This suggests that the overall release kinetics are primarily dictated by the intrinsic properties of the polymer rather than the initial drug concentration within the system.

Diverse tissue engineering applications necessitate specific responses from different cell types, and these responses are directly, and significantly impacted by the strength and elasticity of the scaffolds. The significance of these properties becomes evident when considering cell growth in tissues like cartilage and tendons, which are consistently subjected to shear stresses and compressive loads.<sup>[67]</sup> Mechanical testing of PCL fibres revealed that smaller diameter fibres exhibited higher modulus, with a notable linear increase in modulus for fibres of diameter < 1 µm. However, above this diameter, no significant correlation between fibre diameter and modulus was observed.<sup>[68]</sup> The fibres obtained in a more volatile solvent (i.e., FA:AA) are characterized by rapid drying resulting in a notably distinct microstructure between the surface and bulk regions of the fibre. The surface features highly aligned amorphous regions, whereas the bulk displays lower alignment. As the fibre diameter decreases, the rise in the surface-to-bulk ratio is expected to alter the mechanical properties of the underlying material, leading to an increase in modulus.<sup>[69]</sup> While the material properties of an individual fibre undeniably impact the properties of the resulting scaffold, a direct correlation between them is not evident. In our results the fibres produced in AA were thicker with respect to the ones produced in FA:AA, nevertheless, the latter were characterized by a lower Young's Modulus. The discrepancies of our results with previous works can be attributed to the absence of correlation between the mechanical properties of a single fibre and that of the overall network. This discrepancy is primarily attributed to method-dependent factors such as inter-fibre adhesion<sup>[70]</sup> and curvature.<sup>[71]</sup> These factors influence the interactions between fibres, which, in turn, play a crucial role during fibre reorientation under stress,<sup>[69]</sup> resulting in a mismatch between the mechanics of the scaffold and those of the individual fibres.

The BSA blending in the PCL/AA solution resulted in a reduction of the mechanical properties with respect to the

BSA-free counterpart. Contrastingly, increased mechanical properties were observed after BSA blending in the FA:AA solution. The higher BSA solubility likely fostered robust physical interactions, such as hydrogen bonding and molecular entanglement, between BSA and PCL constituents, leading to the formation of a more rigid nanofibrous structure. Hydrogen bonds between the protein's amine groups and the polymer's carbonyl groups should restrict molecular mobility under mechanical stress, leading to an increase in the fibres' elastic modulus. In the AA-prepared solution, the lower solubility of the protein and larger fibre diameters contributed to spatial separation between polymer chains and protein molecules. This diminished entanglement and intermolecular bonding, resulting in a less ordered and oriented structure with increased molecular freedom, and lower resilience to the applied stress. The FA:AA counterpart, was characterized by a higher elongation at break compared to BSA-free-PCL fibres, potentially attributable to the greater unfolding extent of the amorphous random coil of BSA.

We next analysed the impact of incorporating nanoparticles on the mechanical properties. In both scenarios, there was a decline in mechanical properties attributed to the introduction of MSNs as elements of discontinuity, regarded as the source of crack propagation within the structure of individual fibres.<sup>[72]</sup> This embrittlement was more pronounced for fibres prepared in AA compared to that in FA:AA. As demonstrated in this work, particles were more uniformly distributed throughout the thickness of the fibres in the AA formulation. In contrast, in the FA:AA formulation, particles tended to migrate outward, being excluded by the bulk structure, making only a minimal contribution to the mechanical properties of the fibrous mat.

MSCs and TSCs are robust in vitro models for the investigation of tenogenic differentiation, influenced by scaffold materials, morphologies, and soluble signals. Tenocytes adhere to a well-organized fibrillar collagen matrix, mainly consisting of type-I collagen and small leucine-rich proteoglycans that control the self-assembly of collagen into fibrils. These fibrils, ranging from 40–400 nm, serve as the fundamental subcellular components of collagen, while collagen fibres, measuring 10–50 µm, are the key structural units at the cellular scale, where cells physically engage.<sup>[73]</sup> For this reason, we focused the cell availability and metabolic activity analysis on 20% PCL in AA scaffolds with the incorporation of MSNs. This selection is grounded in the demonstrated capability of micrometre-scale fibres to better emulate the microenvironment naturally surrounding tendon cells.<sup>[73]</sup> Furthermore, the use of micrometre-scale fibres facilitated the incorporation of mesoporous silica particles, intended as carriers for future soluble signals, including growth differentiation factor 7 (GDF-7). The cell attachment and proliferation obtained in our study is consistent not only with the well-known PCL biocompatibility,<sup>[74]</sup> but also with the combination of both MSNs and electrospun fibres. This finding is supported by other research studies where the combination of MSNs and random polymer-based nanofibrous scaffolds led to improved cell adhesion.<sup>[75]</sup> Finally, considering the growing body of research investigating the impact of physiological oxygen levels on the proliferation of both MSCs and TSCs,<sup>[76–79]</sup> this study aimed to compare cellular growth and attachment to the optimised scaffold under 21% O<sub>2</sub> and 2% O<sub>2</sub> conditions, demonstrating improved cellular viability under physiological oxygen concentra-

tions. The combined influence of physiological oxygen tension and structural anisotropy, which closely mimics the native tendon tissue environment, significantly affected the growth and migration of both MSCs and TSCs. As elsewhere demonstrated, aligned nano- and micro-topographies serve as instructive cues, modulating cellular behaviour with an efficacy comparable to that of biochemical signals.<sup>[80]</sup>

## 4. Conclusion

In this study the effects of the challenges of protein incorporation during electrospinning were investigated, revealing insights into the interplay between protein solubility, fibre diameter, and mechanical properties. The use of mesoporous silica nanoparticles further enhanced the functional capabilities of the scaffolds, offering sustained release and protection of bioactive molecules. Our findings demonstrate that the choice of solvents and the use of MSNs as drug carriers are critical for optimizing the encapsulation of drugs in electrospun fibres. Additionally, the study highlights the potential of using micrometre-scale fibres to mimic the natural extracellular matrix, providing a conducive environment for cell growth and differentiation. These advancements pave the way for the development of more effective and versatile growth factor-releasing fibrous biomaterials for tendon tissue engineering applications.

## 5. Experimental Section

**Mesenchymal/Stromal Cells Isolation:** MSCs were isolated from donor bone marrow aspirate retrieved from three donors (two female and one male) aged between 20 and 35 (Lonza, UK). These cells were isolated from donated human tissue after obtaining permission for their use in research applications by informed consent or legal authorization. Heparin was added to bone marrow aspirates to inhibit coagulation. To resuspend the cells, aspirated were mixed gently before seeding. Seeding was performed within 48 h of aspiration to achieve 80–90% mononucleated cell (MNC) viability.<sup>[81]</sup>

Whole bone marrow was seeded at a density of 100 000 MNC cm<sup>-2</sup> on 10 ng mL<sup>-1</sup> fibronectin-coated flasks. MNC were seeded into Dulbecco's-Modified Eagles Medium (DMEM, 4.5 g L<sup>-1</sup> glucose) supplemented with 5% Human Platelet Lysate (StemCell Technologies), 100 U mL<sup>-1</sup> penicillin, 100 U mL<sup>-1</sup> streptomycin, 1% non-essential amino acids (NEAA) and 1% L-Glutamine (all Lonza, UK). The recovery of MSCs was carried out in two different environments: either in humidified incubators with an ambient oxygen concentration of 21%, or in a sealed Invivo2 workstation (Baker Ruskinn) maintained at 37 °C with 7% CO<sub>2</sub> and 2% O<sub>2</sub> concentration. For reduced oxygen culture, media was deoxygenated to 2% (HypoxyCOOL, Baker) to bypass inconsistencies associated with preincubation of media in hypoxic conditions.<sup>[82]</sup> After 7 days half of the culture medium was replaced with fresh media; after 14 days media was replaced completely.

**Tendon Stem Cell isolation:** The isolation of tendon stem cells (TSCs), was performed according to a methodology described previously.<sup>[39]</sup> Flexor tendons were obtained from 6-month-old pigs sourced from a local butchery. The tendon tissue underwent three washes with a sterile phosphate-buffered saline (PBS) solution (Lonza) containing 10% Penicillin-Streptomycin-Amphotericin B (PSA) (Lonza), 1% Gentamicin (Lonza), and 1% Ciprofloxacin (Sigma Aldrich). Following this, it was rinsed once with Hanks' Balanced Salt Solution (HBSS; Lonza) supplemented with 2% PSA, 0.2% Gentamicin, and 0.2% Ciprofloxacin. The cleaned tissue was cut into small pieces and digested overnight at 37 °C with type II Collagenase (Gibco); this reaction was subsequently inhibited by foetal bovine serum (FBS) (Biosera). A 70-µm cell strainer (Falcon) was employed to filter the digested tissues and achieve a single-cell suspension. After centrifugation (350 RCF, 8 minutes), cells were resuspended in

**Table 2.** Electrospinning parameters.

Composition	Voltage	Flow rate	Distance	Temperature	Humidity	Rpm
20%PCL in AA	15 kV	0.4 mL h <sup>-1</sup>	12 cm	25 °C	40%	1500 aligned 500 random
20%PCL in FA:AA (7:3)	18 kV	0.6 mL h <sup>-1</sup>	12 cm	25 °C	25%	1500 aligned 500 random
20%PCL in AA + 3%BSA wt	19 kV	0.5 mL h <sup>-1</sup>	12 cm	25 °C	40%	1500 aligned
20%PCL in FA:AA + 3%BSA wt	25 kV	0.6 mL h <sup>-1</sup>	12 cm	25 °C	25%	1500 aligned
20%PCL in AA + 200 mg MSNs	19 kV	0.8 mL h <sup>-1</sup>	12 cm	25 °C	40%	1500 aligned
20%PCL in FA:AA + +200 mg MSNs	26 kV	0.5 mL h <sup>-1</sup>	12 cm	25 °C	25%	1500 aligned

DMEM (1 g L<sup>-1</sup> glucose) containing L-glutamine, sodium pyruvate (Corning), 15% FBS, 1% PSA, 2.5 ng mL<sup>-1</sup> stem cell factor (SCF; Peprotech), 2.5 ng mL<sup>-1</sup> basic fibroblast growth factor (bFGF; Sigma Aldrich) and 0.4 ng mL<sup>-1</sup> epidermal growth factor (EGF; Sigma Aldrich). A mycoplasma removal agent (MRA; Bio-Rad) at 0.1 µg mL<sup>-1</sup> was included in the medium for the first 2 weeks.

Cells were seeded at a density of  $52 \times 10^2$  cells per cm<sup>2</sup> and cultured at 37 °C under either atmospheric oxygen concentration (21%) or physiological oxygen concentration (2%). After 48 h, nonadherent debris was removed by washing the wells twice. The cells attained confluence in seven days, thus they were enzymatically detached with 0.05% (w/v) trypsin/0.02% (w/v) ethylenediaminetetraacetic acid (EDTA) (LONZA), designated as passage 0 and cryopreserved for later experiments.

**PCL Fibre Preparation and Characterization:** Micro-fibres were fabricated by electrospinning with a commercial electrospinning apparatus (IME Medical Electrospinning, Waalre, The Netherlands). This device is equipped with a climate-controlled chamber (EC-CLI) and a gas shield accessory. Briefly, the synthetic polymer, Poly-ε-caprolactone (PCL), with molecular weight (M<sub>w</sub>) of 80 kDa (Sigma-Aldrich) was solubilized in two different solvent systems. The first constituted by acetic acid (VWR, Darmstadt, Germany), the second by formic acid (VWR, Darmstadt, Germany) and acetic acid at a 7:3 ratio. A 20% PCL solution was used to produce aligned and random electrospun fibres.

To synthesize the BSA/PCL fibres, BSA (3 wt.% with respect to polymer mass) was co-dissolved in the above-mentioned PCL/AA/FA:AA solutions and stirred for 1 h. The solutions were sonicated for a further hour before electrospinning.

For particle incorporation, 200 mg of MSNs were mixed with the polymer solution and sonicated (140 W, Ultrasonic bath, Bandelin Sonorex) for 1 h. The solution compositions and electrospinning parameters for the different classes of fibres are presented in **Table 2**.

The fibres' morphology was evaluated using scanning electron microscopy (SEM; Zeiss Auriga 4750, Carl-Zeiss, Jena, Germany) combined with energy dispersive X-ray spectroscopy (EDS, X-MaxN Oxford Instruments, UK). Prior to imaging, samples were coated with a thin layer of gold via sputtering. Fibre diameter distribution and alignment were analysed with ImageJ software (NIH, USA). Fibre orientation was analysed using the Directionality plugin in ImageJ, which quantifies the predominant alignment of structures by assessing the angular distribution of detected edges within the image. A corresponding colour map assigns orientation values to individual fibres, while a directionality histogram provides a quantitative representation of the angular distribution across the sample.

Characteristic PCL and BSA functional groups were detected via Fourier transform infrared spectroscopy (ATR-FTIR; SHIMADZU, Japan). It was performed in absorbance mode, covering a spectral range of 4000–400 cm<sup>-1</sup>, at a resolution of 4 cm<sup>-1</sup> and a scanning speed of 40 scans per minute. The wettability of the scaffolds was assessed by measuring the water contact angle using an optical tensiometer (Attension Theta Lite, Bilin Scientific) and analysing the results with the Young-Laplace method. A 10 µL water droplet was deposited onto the scaffold surface, and the sessile drop was recorded for subsequent analysis.

**Synthesis and Characterisation of Mesoporous Silica Nanoparticles:** MSNs were produced via a microemulsion-assisted sol-gel technique.<sup>[83]</sup> Reaction parameters have been selected post-optimization (see S.2, Supporting Information). Initially, 1.12 g of hexadecyltrimethylammonium bromide (CTAB; MW: 364.45 g mol<sup>-1</sup>, Sigma Aldrich) was dissolved in 52 mL of deionized water with continuous stirring at 37 °C for 30 min. Following this, 16 mL of ethyl acetate was gradually added to the mixture while maintaining stirring for another 30 min. Ammonium hydroxide (28% ammonia solution; MW: 17.03 g mol<sup>-1</sup>, density: 0.90 kg L<sup>-1</sup>, VWR) was then introduced to adjust the pH to a range of 9–10.5. After allowing the solution to equilibrate for 15 min, 6.217 mL of tetraethyl orthosilicate (TEOS; MW: 208.33 g mol<sup>-1</sup>, Sigma Aldrich) were added, and the reaction was left to proceed under stirring for 4 h. The nanoparticles were separated by centrifugation at 7000 rpm for 5 min using a Centrifuge 5430R (Eppendorf, Germany). The recovered material was washed twice with water and once with ethanol to remove residual reactants, followed by drying at 60 °C for 24 h. To enhance the structural integrity of the nanoparticles, they were calcined at 700 °C for 2 h at a heating rate of 2 °C min<sup>-1</sup>.

Morphological analyses were conducted using scanning electron microscopy (SEM; Zeiss Auriga 4750). For imaging, the nanoparticles were dispersed in ethanol and deposited onto aluminium stubs without additional coating. Particle size distribution was analysed using ImageJ software (NIH, USA).

**BSA Loading and Release From MSNs:** BSA has been shown in prior studies to protect the bioactivity of growth factors in a dose-dependent manner.<sup>[84–86]</sup> Therefore, this model protein was chosen as the starting point to investigate the encapsulation and release properties of MSNs. BSA was loaded into MSNs using various BSA-to-particle concentration ratios to optimize encapsulation efficiency (EE), with the highest efficiency achieved at a 30:40 BSA-to-MSNs ratio. The interaction with BSA was intended to shield growth factors from degradation during electrospinning in combination with the use of green solvents to further preserve the secondary structure.

For encapsulation, solutions were left under magnetic stirring for 24 h before centrifugation. The supernatant was analysed to obtain the encapsulation efficiency:

$$EE\% = \frac{c_i - c_{\text{supernatant}}}{c_i} \quad (1)$$

where  $c_i$  is the initial drug concentration and  $c_{\text{supernatant}}$  is the supernatant concentration after encapsulation. Isolated particles were dried at 37 °C or freeze-dried for 24 h. After drying, the Loading Capacity (LC%) was determined:

$$LC\% = \frac{\text{weight of drug encapsulated}}{\text{weight of nanoparticles after loading}} \times 100 \quad (2)$$

Attenuated total reflection-fourier transform infrared spectroscopy (ATR-FTIR; IRAffinity-1S spectrophotometer, SHIMADZU) was employed to identify characteristic absorption spectra of silica and BSA-loaded MSNs. ATR-FTIR measurements were conducted in absorbance mode,

spanning a wavenumber range of 4000–400 cm<sup>−1</sup>, with a scan speed of 40 scans per min and a resolution of 4 cm<sup>−1</sup>.

To determine whether MSNs could deliver the adsorbed BSA under physiological conditions, 10 mg of particles were re-suspended in 10 mL PBS (pH 7) and left under rotation at 37 °C. At predetermined times (every hour for the first burst release, and every day in the subsequent period) the samples were subjected to centrifugation to pellet the particles. At each time point, 10% of the whole supernatant was removed and the concentration of released BSA was determined using a Bradford reagent (Sigma-Aldrich) assay; 0.3 mL of Bradford reagent was added to 10 µL aliquot sample. The optical density of the solution was measured at 595 nm using a UV–vis spectrophotometer. The volume of supernatant removed was replaced with fresh PBS. The calibration curve was performed with standard concentrations of BSA in PBS with a relative amount of nonloaded MSNs particles, to balance any contribution of the particles to the absorption at 595 nm. Release experiments were performed in triplicate. Cumulative drug release was calculated as follows:

$$\text{Cumulative percentage release (\%)} = \frac{\text{volume of sample withdrawn}}{\text{total supernatant volume}} \times P(t-1) + P_t \quad (3)$$

with  $P_t$  the percentage releases at time  $t$ , and  $P(t-1)$  the percentage of drug release in all the previous time points. Fractional sampling and sink conditions analysis were selected for any specific molecule based on the sensitivity of the assay utilised.

N<sub>2</sub> adsorption-desorption isotherms at 77 K were conducted using a Quantachrome ASiQwin gas adsorption analyser (Quantachrome Instruments) to evaluate the surface area and pore size distribution before and after BSA encapsulation. Prior to measurements, samples were degassed under a vacuum at 300 °C for 12 h. The surface area was calculated using the Brunauer–Emmet–Teller method, while the pore size distribution was determined using the Barrett–Joyner–Halenda method.

Finally, the surface charge of particles before and after BSA encapsulation was determined using a Zetasizer dyn device (Malvern). The measurements were performed in ethanol at pH 7, with a particle concentration of 0.1 mg mL<sup>−1</sup>. After 10 min of sonication the samples were analysed.

**Lysozyme and GDF-7 Loading and Release From MSNs:** Lysozyme encapsulation in MSNs was performed in a solution at 200 µg mL<sup>−1</sup> of lysozyme (ThermoScientific) and 10 mg mL<sup>−1</sup> of particles in dH<sub>2</sub>O. Solutions were left under magnetic stirring for 24 h before centrifugation. The supernatant was analysed to obtain the encapsulation efficiency as previously described. Isolated particles were freeze-dried and used for the release analysis. Particles were re-suspended in 10 mL PBS (pH 7) and left under rotation at 37 °C temperature. At each time point, the PBS was removed for release analysis and substituted with fresh PBS (sink conditions). Bradford reagent (Sigma-Aldrich) assay was used to detect the release of Lysozyme; 150 µL of Bradford reagent was added to 150 µL aliquot sample. The optical density of the solution was measured at 595 nm using a UV–vis spectrophotometer. The calibration curve was performed with standard concentrations of lysozyme in PBS.

To load GDF-7 (Recombinant Human GDF-7, PeproTech) into MSNs, 2 mg of particles were added to 1 mL of 16.7 µg mL<sup>−1</sup> GDF-7 in deionised water and vortexed in the dark for 24 h at room temperature. The MSNs were then centrifuged at 1400 rpm for 20 min to separate the MSNs from the supernatant. The GDF-7 concentration in the supernatant was determined by measuring the O.D. absorbance at 450 nm and comparing it to the standard curve. Encapsulation efficiency and loading capacity were calculated based on the free GDF-7 concentration. After centrifugation, the particles were freeze-dried. Loaded particles were used for release analysis

in a suspension at 1 mg mL<sup>−1</sup> of particles. At each time point, 10% of the solution was extracted for release measurements and replaced with the same quantity of fresh PBS. Human GDF-7 ELISA Kit 96T (Hoelzel biotech) was used to detect the released growth factor per the manufacturer's instructions. The encapsulation efficiency and cumulative release for both lysozyme and GDF-7 were calculated using Equations (1) and (3), respectively.

To determine the lysozyme release kinetically, the release profile was compared with the following models:

Zero Order kinetic:<sup>[87]</sup>

$$Q_t = Q_0 + K_0 t \quad (4)$$

First order kinetic:<sup>[37]</sup>

$$\log C = \log C_0 - Kt/2.303 \quad (5)$$

Higuchi Model:<sup>[88]</sup>

$$Q = K_H \times t^{1/2} \quad (6)$$

Korsmeyer-Peppas Model:<sup>[89]</sup>

$$\log \frac{M}{M_\infty} = \log K_p + n \log t \quad (7)$$

where  $Q_t$  is the amount of drug dissolved in time  $t$ ,  $Q_0$  is the initial amount of drug in the solution (generally equal to zero),  $K_0$  is the zero-order release constant,  $C$  is the percentage of drug remaining in the delivery system,  $C_0$  is the initial concentration of drug,  $K$  is the first-order rate constant,  $Q$  is the percentage of drug released at time  $t$ ,  $K_H$  is the Higuchi dissolution constant,  $\frac{M}{M_\infty}$  is the fraction of drug release at time  $t$ ,  $K_p$  the drug release constant and  $n$  is the release exponent. These models were applied to investigate the release profiles in all subsequent experiments related to release.

**Fibre Plasma Treatment:** The electrospun polymer meshes were treated with low-pressure air plasma using a laboratory plasma system (Diener Electronics – Femto). Plasma was generated with a low-frequency (LF) plasma generator operating at 40 kHz and an adjustable power range of 0–100 W. Samples were placed centrally on a Petri dish inside the chamber. The treatment parameters, exposure time and generator power, were set to optimize the process. Each side of the samples underwent plasma exposure for 50 s at a fixed generator power of 25 W.

**Lysozyme Release and Activity From MSN-Loaded Fibres:** Before analysing the release profile of lysozyme-loaded MSNs embedded within electrospun fibres, lysozyme was directly encapsulated into aligned 20% PCL fibres fabricated in AA. This approach aimed to evaluate potential conformational changes in the molecule's tertiary structure. A lysozyme concentration equivalent to 50% of the polymer mass was used, and ATR-FTIR analysis was conducted in absorbance mode, covering a spectral range of 4000–400 cm<sup>−1</sup>, at a resolution of 4 cm<sup>−1</sup> and a scanning speed of 40 scans per minute.

Lysozyme encapsulation in MSNs was performed as previously described in Section 2.5. After freeze-drying 50 mg of lysozyme-loaded MSNs particles were mixed with 20% PCL in AA polymer solution and sonicated (140 W, Ultrasonic bath, Bandelin Sonorex) for 1 h, and electrospun with parameter detailed in Table 3.

**Table 3.** Regression coefficient ( $R^2$ ) of four different kinetic models fitted to the lysozyme release from composite fibres.

Model	Korsmeyer-Peppas ( $R^2$ )	$n$	Zero-order ( $R^2$ )	First-order ( $R^2$ )	Higuchi ( $R^2$ )
Sample					
Lysozyme-loaded MSNs embedded in 20%PCL aligned fibres	0.9974	0.34	0.8712	0.9791	0.9653



After plasma treatment, 150 mg of fibres were placed in 5 mL of PBS (pH 7) and left at 37 °C in a shaking incubator. At each time point, the entire volume was removed for release analysis and substituted with 5 mL of fresh PBS (sink conditions). Bradford reagent (Sigma-Aldrich) assay was used to detect the release of lysozyme. EnzChek Lysozyme Assay Kit (Invitrogen) was used to assess the lysozyme activity after release. Concentration standards were prepared for the calibration curve. To 50 µL of standard/samples, were added 50 µL of a 50 µg mL<sup>-1</sup> DQ lysozyme substrate fluorescein conjugate. The mixture was incubated for 30 min at 37 °C, protected from light. Fluorescence was measured in a fluorescence microplate reader using excitation/emission of 485/530 nm. The background was corrected by subtracting the measured values from the no-enzyme control. The activity was plotted as u mL<sup>-1</sup>.

**Mechanical Tests:** Tensile tests were performed in triplicate in each condition (aligned PCL fibres, BSA-loaded fibres and BSA-loaded MSNs embedded in aligned fibres) using a Testometric x250 testing machine equipped with a 25 kgf load cell. Tensile specimens (length: 2 cm and width: 0.5 cm) were prepared by anchoring the membrane to a paper frame for better handling and avoiding any fibre slippage in the machine fixtures, cutting the frame before the test started. For each scaffold, the thickness and area of the fibrous mat were assessed. To evaluate the mat thickness, the overall thickness of the fibrous mat was measured in two different equidistant zones with a calliper and measurements were averaged. The area evaluation was determined on the supporting paper for handling ease. These were scanned at a resolution of 600 dpi to ensure high-edge precision. A ruler was placed on the scanning plane to verify that there was no scaling during the copy. Subsequently, the scans were imported into Image J and, for each, the correlation between pixels and millimetres was assessed. A binary mask was generated to segment and convert the images into logical classes. The images were then analysed to obtain the area in pixels and converted to cm<sup>2</sup>.

Tensile tests were performed at a rate of 5 mm min<sup>-1</sup> with a pre-tension of 0.02 N. During the experimental phase, force-displacement data were collected, and stress-strain curves were obtained by determining the engineering stress,  $\sigma$ , as the force divided by the area of the meshes' cross-section. The strain  $\epsilon$ , was calculated by normalizing the displacement in relation to the initial length of the samples, according to the following ratio:

$$\sigma = \frac{F}{A} \quad (8)$$

$$\epsilon = \frac{\Delta L}{L_0} \quad (9)$$

where F is the measured force, A is the mesh cross-sectional area,  $\Delta L$  is the change in length, and  $L_0$  is the gauge length of the samples. The elastic modulus (Young's Modulus) was derived from a linear best-fit line with a 0.2% offset in the linear region. Strain at failure is defined as the strain at which the fibres undergo rupture.

**Cell Viability Assessment: Live/Dead and Alamar Blue Sssays:** Cell viability was performed by seeding on 20% PCL fibres obtained in AA with encapsulated particles at 20% weight with respect to the polymer. Fibres were placed on PLA rings, through heat adhesion resulting in a total surface area of 0.24 cm<sup>2</sup>.

Prior to cell seeding, all fibres were plasma treated to increase hydrophilicity and promote cell attachment. MSCs were seeded at 10 000 cells per scaffold, TSCs at 5500 cells per scaffold. Cells were seeded in 100 µL of media and left overnight to allow the attachment. The following day samples were flooded with a full volume of cell culture media.

Cell metabolism was quantitatively evaluated using Alamar Blue (Thermo Fisher Scientific) according to the manufacturer's instructions. At 1, 7, and 14 day time points, the MSCs and TSCs medium was removed from five replicates and transferred to a fresh 48-well plate. The samples were then incubated with 300 µL of fresh culture medium containing 10%(v/v) of Alamar Blue solution for 4 h at 37 °C with 5% CO<sub>2</sub> and either 21% O<sub>2</sub> or 2% O<sub>2</sub>. Following incubation, three 100 µL aliquots of media from each sample were transferred to 96-well plates. Sample flu-

orescence was read at 560/590 nm(excitation/emission) using a UV spectrophotometer.

The distribution of viable and non-viable cells adhered to the scaffolds was assessed by Live/Dead assay. Following 1, 7, and 14 days of cell seeding, samples were transferred to a new 48-well plate and rinsed with PBS. The disk samples were incubated for 1 h in 200 µL of LIVE/DEAD staining solution (ThermoFisherScientific, Invitrogen) in PBS containing 2 µM Calcein and 4 µM SYTOX Deep Red Nucleic Acid Stain. The stained samples were imaged with a confocal microscope immediately after the staining.

## Supporting Information

Supporting Information is available from the Wiley Online Library or from the author.

## Acknowledgements

This paper is a part of the dissemination activities of the project P4FIT. This project received funding from the European Union's Horizon 2020 Research and Innovation Program under the Marie Skłodowska-Curie [grant agreement number 955685].

## Conflict of Interest

The authors declare no conflict of interest.

## Data Availability Statement

The data that support the findings of this study are available from the corresponding author upon reasonable request.

## Keywords

drug delivery system, electrospinning, mesenchymal/stromal stem cells, mesoporous silica nanoparticles, tendon progenitor stem cells, tendon tissue engineering

Received: February 5, 2025

Revised: March 24, 2025

Published online:

- [1] A. Guevara-Alvarez, A. Schmitt, R. P. Russell, A. B. Imhoff, S. Buchmann, *Muscles Ligaments Tendons J.* **2014**, 4, 378.
- [2] C. N. Maganaris, M. V. N., M. N., *Disab. Rehab.* **2008**, 30, 1542.
- [3] M. Chatterjee, P. M. Muljadi, N. Andarawis-Puri, *Connect. Tissue Res.* **2022**, 63, 28.
- [4] V. L. Tsang, S. N. Bhatia, *Adv. Biochem. Eng. Biotechnol.* **2005**, 103, 189.
- [5] L. M. Galatz, L. Gerstenfeld, E. Heber-Katz, S. A. Rodeo, *J. Orthop. Res.* **2015**, 33, 823.
- [6] P. P. Y. Lui, *Stem Cells Cloning: Adv. Appl.* **2015**, 8, 163.
- [7] M. F. Pietschmann, B. Frankewycz, P. Schmitz, D. Docheva, B. Sievers, V. Jansson, M. Schieker, P. E. Müller, *J. Mater. Sci. Mater. Med.* **2013**, 24, 211.
- [8] M. Iannone, M. Ventre, L. Formisano, L. Casalino, E. J. Patriarca, P. A. Netti, *Nano Lett.* **2015**, 15, 1517.
- [9] S. Xie, Y. Zhou, Y. Tang, C. Chen, S. Li, C. Zhao, J. Hu, H. Lu, *J. Orthop. Res.* **2019**, 37, 887.

- [10] N. Iwasaki, M. Roldo, A. Karali, A. Sensini, G. Blunn, *Eng. Regen.* **2024**, 5, 409.
- [11] M. Govoni, A. C. Berardi, C. Muscare, R. Campardelli, F. Bonafè, C. Guarnieri, E. Reverchon, E. Giordano, N. Maffulli, G. D. Porta, *Tissue Eng. Part A* **2017**, 23, 811.
- [12] R. I. Sharma, J. G. Snedeker, *Biomaterials* **2010**, 31, 7695.
- [13] J. Xue, T. Wu, Y. Dai, Y. Xia, *Chem. Rev.* **2019**, 119, 5298.
- [14] Q. Yang, J. Li, W. Su, L. Yu, T. Li, Y. Wang, K. Zhang, Y. Wu, L. Want, *Front. Bioeng. Biotechnol.* **2022**, 10, 1474.
- [15] D. Li, Y. Xia, *Adv. Mater.* **2004**, 16, 1151.
- [16] M. Eslamian, M. Khorrami, N. Yi, S. Majd, M. R. Abidian, *J. Mater. Chem. B* **2019**, 7, 224.
- [17] M. Eslamian, F. Mirab, V. K. Raghunathan, S. Majd, M. R. Abidian, *Adv. Funct. Mater.* **2021**, 31, 1.
- [18] D. J. Murphy, A. J. Nixon, *Am. J. Vet. Res.* **1997**, 58, 103.
- [19] K. B. Sugg, J. F. Markworth, N. P. Disser, A. M. Rizzi, J. R. Talarek, D. C. Sarver, S. V. Brooks, C. L. Mendias, *Am. J. Physiol. Cell Physiol.* **2018**, 314, C389.
- [20] A. E. Brent, C. J. Tabin, *Development* **2004**, 131, 3885.
- [21] S. P. Berasi, U. Varadarajan, J. Archambault, M. Cain, T. A. Souza, A. Abouzeid, J. Li, C. T. Brown, A. J. Dorner, H. J. Seeherman, S. A. Jelinsky, *Groundwater* **2011**, 29, 128.
- [22] H. Li, S. Luo, H. Wang, Y. Chen, M. Ding, J. Lu, L. i. Jiang, K. Lyu, S. Huang, H. Shi, H. Chen, S. Li, *Injury* **2023**, 54, 111052.
- [23] J. B. Tang, Y. F. Wu, Y. Cao, C. H. Chen, Y. L. Zhou, B. Avanesian, M. Shimada, X. T. Wang, P. Y. Liu, *Sci. Rep.* **2016**, 6, 1.
- [24] H. Shen, R. H. Gelberman, M. J. Silva, S. E. Sakiyama-Elbert, S. Thomopoulos, *PLoS ONE* **2013**, 8, 77613.
- [25] T. Arakawa, S. J. Prestrelski, W. C. Kenney, J. F. Carpenter, *Adv. Drug Deliv. Rev.* **2001**, 46, 307.
- [26] E. Walter, K. Moelling, J. Pavlovic, H. P. Merkle, *J. Controlled Release* **1999**, 61, 361.
- [27] F. Rizzi, R. Castaldo, T. Latronico, P. Lasala, G. Gentile, M. Lavorgna, M. Striccoli, A. Agostiano, R. Comparelli, N. Depalo, M. L. Curri, E. Fanizza, *Molecules* **2021**, 26, 4247.
- [28] E. M. Abdelrazek, A. M. Hezma, A. El-khodary, A. M. Elzayat, *Egypt. J. Basic Appl. Sci.* **2016**, 3, 10.
- [29] H. Xu, N. Yao, H. Xu, T. Wang, G. Li, Z. Li, *Int. J. Mol. Sci.* **2013**, 14, 14185.
- [30] P. Wen, Y. Wen, X. Huang, M. H. Zong, H. Wu, *J. Agric. Food Chem.* **2017**, 65, 4786.
- [31] E. Vanea, K. Magyari, V. Simon, *J. Optoelectron. Adv. Mater.* **2010**, 12, 1206.
- [32] N. Rameli, K. Jumbri, R. A. Wahab, A. Ramli, F. Huyop, *J. Phys. Conf. Ser.* **2018**, 1123, 012068.
- [33] M. Thommes, K. Kaneko, A. V. Neimark, J. P. Olivier, F. Rodriguez-Reinoso, J. Rouquerol, K. S. W. Sing, *Pure Appl. Chem.* **2015**, 87, 1051.
- [34] J. Ho, M. K. Danquah, H. Wang, G. M. Forde, *J. Chem. Technol. Biotechnol.* **2008**, 83, 351.
- [35] E. D. N. S. Abeyrathne, H. Y. Lee, D. U. Ahn, *Poult. Sci.* **2013**, 92, 3292.
- [36] I. El Bialy, W. Jiskoot, M. Reza Nejadnik, *Pharm. Res.* **2017**, 34, 1152.
- [37] *Strategies to Modify the Drug Release from Pharmaceutical Systems*, Elsevier, Amsterdam **2015**, p. 63.
- [38] Z. Lin, H. Chen, S. Li, X. Li, J. Wang, S. Xu, *Polymers (Basel)* **2023**, 15, 2318.
- [39] M. Clerici, V. Citro, A. L. Byrne, T. P. Dale, A. R. Boccaccini, G. Della Porta, N. Maffulli, N. R. Forsyth, *Int. J. Mol. Sci.* **2023**, 24, 15107.
- [40] A. Moreira, D. Lawson, L. Onyekuru, K. Dziemidowicz, U. Angkawitwong, P. F. Costa, N. Radacs, G. R. Williams, *J. Control Release* **2021**, 329, 1172.
- [41] C. Jacobsen, P. J. García-Moreno, A. C. Mendes, R. V. Mateiu, I. S. Chronakis, *Annu. Rev. Food Sci. Technol.* **2018**, 9, 525.
- [42] A. S. Mistry, Q. P. Pham, C. Schouten, T. Yeh, E. M. Christenson, A. G. Mikos, J. A. Jansen, *J. Biomed. Mater. Res.* **2009**, 92A, 451.
- [43] A. Akhmetova, A. Heinz, *Pharmaceutics* **2021**, 13, 1.
- [44] G. Houen, *Acta Chem. Scand.* **1996**, 50, 68.
- [45] A. Dong, P. Huang, W. S. Caughey, *Biochemistry* **1990**, 29, 3303.
- [46] T. Estey, J. Kang, S. P. Schwendeman, J. F. Carpenter, *J. Pharm. Sci.* **2006**, 95, 1626.
- [47] G. Zhu, S. R. Mallery, S. P. Schwendeman, *Nat. Biotechnol.* **2000**, 18, 52.
- [48] C. Xu, M. Yu, O. Noonan, J. Zhang, H. Song, H. Zhang, C. Lei, Y. Niu, X. Huang, Y. Yang, C. Yu, *Small* **2015**, 11, 5949.
- [49] C. Xu, Y. Niu, A. Popat, S. Jambhrunkar, S. Karmakar, C. Yu, *J. Mater. Chem. B* **2013**, 2, 253.
- [50] C. Xu, C. Lei, L. Huang, J. Zhang, H. Zhang, H. Song, M. Yu, Y. Wu, C. Chen, C. Yu, *Chem. Mater.* **2017**, 29, 7725.
- [51] P. L. Abbaraju, A. K. Meka, S. Jambhrunkar, J. Zhang, C. Xu, A. Popat, C. Yu, *J. Mater. Chem. B* **2014**, 2, 8298.
- [52] C. Xu, J. Xu, L. Xiao, Z. Li, Y. Xiao, M. Dargusch, C. Lei, Y. He, Q. Ye, *RSC Adv.* **2018**, 8, 16503.
- [53] X. Chun, C. Lei, Y. Chengzhong, *Front. Chem.* **2019**, 7, 290.
- [54] C. Lei, O. Noonan, S. Jambhrunkar, K. Qian, C. Xu, J. Zhang, A. Nouwens, C. Yu, *Small* **2014**, 10, 2413.
- [55] Z. A. Allothman, *Materials* **2012**, 5, 2874.
- [56] S. M. Shawky, A. A. Abo-ALHassan, H. Lill, D. Bald, S. F. EL-Khamisy, E.-Z. M. Ebeid, *J. Nanosci.: Curr. Res.* **2016**, 1, 1.
- [57] M. Thommes, *Chem. Ing. Tech.* **2010**, 82, 1059.
- [58] Z. A. Allothman, *Materials* **2012**, 5, 2874.
- [59] J. Meissner, A. Prause, B. Bharti, G. H. Findenegg, *Colloid Polym. Sci.* **2015**, 293, 3381.
- [60] C. A. Haynes, W. Norde, *Coll. Surf B Biointerf.* **1994**, 2, 517.
- [61] R. Li, Z. Wu, Y. Wang, L. Ding, Y. Wang, *Biotechnol. Rep.* **2016**, 9, 46.
- [62] A. L. Ajiboye, V. Trivedi, J. Mitchell, *Drug Dev. Ind. Pharm.* **2020**, 46, 576.
- [63] K. C. Kao, T. S. Lin, C. Y. Mou, *J. Phys. Chem. C* **2014**, 118, 6734.
- [64] Y. Liu, Q. Guo, X. Zhang, Y. Wang, X. Mo, T. Wu, *Adv. Fiber Mater.* **2023**, 5, 1241.
- [65] L. Xu, W. Li, S. Sadeghi-Soureh, S. Amirsadad, R. Pourpirali, S. Alijani, *J. Biomed. Mater. Res. A* **2022**, 110, 316.
- [66] K. Qiu, C. He, W. Feng, W. Wang, X. Zhou, Z. Yin, L. Chen, H. Wang, X. Mo, *J. Mater. Chem. B* **2013**, 1, 4601.
- [67] G. H. Kim, *Biomed. Mater.* **2008**, 3, 025010.
- [68] D. Alexeev, N. Goedecke, J. Snedeker, S. Ferguson, *Mater. Today Commun.* **2020**, 24, 101211.
- [69] D. Alexeev, N. Goedecke, J. Snedeker, S. Ferguson, *Mater. Today Commun.* **2020**, 24, 101211.
- [70] S. J. Lee, S. H. Oh, J. Liu, S. Soker, A. Atala, J. J. Yoo, *Biomaterials* **2008**, 29, 1422.
- [71] C. L. Pai, M. C. Boyce, G. C. Rutledge, *Polymer (Guildf)* **2011**, 52, 6126.
- [72] H. M. Lin, Y. H. Lin, F. Y. Hsu, *J. Mater. Sci. Mater. Med.* **2012**, 23, 2619.
- [73] J. G. Snedeker, J. Foolen, *Acta Biomater.* **2017**, 63, 18.
- [74] M. Herrero-Herrero, S. Alberdi-Torres, M. L. González-Fernández, G. Vilarinho-Feltrer, J. C. Rodríguez-Hernández, A. Vallés-Lluch, V. Villar-Suárez, *Polym. Test.* **2021**, 103, 107364.
- [75] M. Mehrasa, M. A. Asadollahi, B. Nasri-Nasrabadi, K. Ghaedi, H. Salehi, A. Dolatshahi-Pirouz, A. Arpanaei, *Mater. Sci. Eng., C* **2016**, 66, 25.
- [76] W. Y. W. Lee, P. P. Y. Lui, Y. F. Rui, *Tissue Eng. Part A* **2011**, 18, 484.
- [77] A. Nowak-Stępniewska, P. N. Osuchowska, H. Fiedorowicz, E. A. Trafny, *Stem Cells Int.* **2022**, 2022, 8775591.

- [78] L. B. Buravkova, E. R. Andreeva, V. Gogvadze, B. Zhivotovsky, *Mitochondrion* **2014**, 19, 105.
- [79] Y. Yu, Y. Zhou, T. Cheng, X. Lu, K. Yu, Y. Zhou, J. Hong, Y. Chen, *Cell Prolif.* **2016**, 49, 173.
- [80] Z. Yin, X. Chen, J. L. Chen, W. L. Shen, T. M. Hieu Nguyen, L. Gao, H. W. Ouyang, *Biomaterials* **2010**, 31, 2163.
- [81] G. S. Kao, H. T. Kim, H. Daley, J. Ritz, S. R. Burger, L. Kelley, C. Vierra-Green, S. Flesch, S. Spellman, J. Miller, D. Confer, *Transfusion* **2011**, 51, 137.
- [82] N. R. Forsyth, R. Steeg, M. Ahmad, M. Al Zubaidi, R. Al-Jumaily, M. Merkhani, T. Dale, *Mimicking Physiological Oxygen in Cell Cultures*, Springer, Berlin **2018**, pp. 129–137.
- [83] Q. Liang, Q. Hu, G. Miao, B. Yuan, X. Chen, *Mater. Lett.* **2015**, 148, 45.
- [84] D. Qu, J. P. Zhu, H. R. Childs, H. H. Lu, *Acta Biomater.* **2019**, 93, 111.
- [85] S. Y. Chew, J. Wen, E. K. F. Yim, K. W. Leong, *Biomacromolecules* **2005**, 6, 2017.
- [86] G. Zhu, S. R. Mallery, S. P. Schwendeman, *Nat. Biotechnol.* **2000**, 18, 52.
- [87] C. G. Varelas, D. G. Dixon, C. A. Steiner, *J. Controlled Release* **1995**, 34, 185.
- [88] T. Higuchi, *J. Pharm. Sci.* **1963**, 52, 1145.
- [89] R. W. Korsmeyer, R. Gurny, E. Doelker, P. Buri, N. A. Peppas, *Int. J. Pharm.* **1983**, 15, 25.